

# Bone refilling in bone multicellular units: Insights into tetracycline data from a computational model

Pascal R Buenzli,<sup>1</sup> Peter Pivonka, David W Smith

Faculty of Engineering, Computing & Mathematics,  
The University of Western Australia, WA 6009, Australia

August 31, 2012

**Abstract** – Bone remodelling is carried out by ‘bone multicellular units’ (BMUs) in which active osteoclasts and active osteoblasts are spatially and temporally coupled. Bone gain or bone loss from remodelling is directly related to the bone balance of individual BMUs. Whilst tetracycline double labelling experiments can reveal part of the dynamics of the refilling process taking place in the ‘closing cone’ of a BMU, less is known about how bone refilling is regulated in a BMU. Here, we extend our previous mathematical model of cell development within a single BMU to investigate the dynamics of refilling in the BMU and help elucidate the contributions to the refilling rate of osteoblast number and osteoblast secretory activity at various positions along the BMU’s length. The mathematical model is based on biochemical coupling between osteoclasts and osteoblasts of various maturity, and includes the differentiation of osteoblasts into osteocytes and bone lining cells, as well as the influence of BMU cavity shrinkage on osteoblast development and activity. The model is calibrated against experimental data on cell densities and cell numbers in a BMU, and compared with other sources of experimental data for validation, such as tetracycline double labelling data. Our model shows that tetracycline double labelling does not reveal the start and the end of the refilling process in a BMU. This suggests that at a particular bone site undergoing remodelling, bone formation starts and ends rapidly, supporting the hypothesis that osteoblasts behave synchronously. Our model also suggests that part of the observed cross-sectional variability in tetracycline data may be due to different bone sites being remodelled by BMUs at different stages of their lifetime. The different stages of a BMU’s lifetime (such as initiation stage, progression stage, and termination stage) depend on whether the cell populations within the BMU are still developing or have reached a quasi-steady state while travelling through bone. We find that due to their longer lifespan, active osteoblasts reach a quasi-steady distribution more slowly than active osteoclasts. We suggest that this fact may locally enlarge the Haversian canal diameter (due to a local lack of osteoblasts compared to osteoclasts) near the BMU’s point of origin.

**Key words:** bone remodeling, bone multicellular unit, closing cone, matrix apposition rate, tetracycline labeling, computational modeling

## 1 Introduction

Bone remodelling renews bone tissue in a spatially and temporally discrete fashion by means of ‘basic multicellular units’ (BMUs). In a BMU, osteoclasts (bone-resorbing cells) create a resorption cavity called the ‘cutting cone’ and osteoblasts (bone-forming cells) refill this cavity, forming a so-called ‘closing cone’ [1, 2]. The action of osteoclasts and osteoblasts in a BMU is well coordinated such that bone formation closely follows bone resorption [1, 3, 4]. During remodelling, bone may be either gained or lost depending on the balance of bone turned over in a BMU, *i.e.*, the amount of bone refilled compared to the amount of bone resorbed. Several disorders of bone remodelling are associated with bone imbalance in BMUs. For example, bone loss in osteoporosis is associated with a negative bone balance that is mainly due to an under-refilling of the BMU cavity opened up by the osteoclasts [3–6]. Bone gain in sclerosing bone disorders such as sclerosteosis, van Buchem disease, and high-bone mass phenotype are associated with a positive bone balance due to increased bone formation [7].

The rate of bone formation is determined both by the number of active osteoblasts and their level of secretory activity

(*i.e.*, the volume of osteoid secreted per unit time by an osteoblast) [3, 8]. Whilst bone formation rate in BMUs has been extensively studied using histomorphometry techniques such as double tetracycline labelling [9–16], much less is known of the respective contributions of osteoblast number and osteoblast level of activity in a BMU *in vivo* [17–20]. Understanding how these respective contributions are evolving in a BMU is necessary to improve our fundamental knowledge of the regulation of bone formation, and so of bone balance in a BMU. These insights are important for our understanding of the development of osteoporosis and for its treatment [5].

Bone refilling is known to have a different dynamics in cortical BMUs, in which matrix apposition rate decreases exponentially in time, than in trabecular BMUs, in which matrix apposition rate decreases linearly in time [1, 15, 20, 21]. In Ref. [21], Martin attempted to explain this difference by assuming that the different geometries of cortical BMUs (cylindrical) and trabecular BMUs (trench-like or planar) would affect the strength of a hypothetical regulatory signal on active osteoblasts produced by osteocytes [22]. Martin’s model does not take into account the number of osteoblasts and their level of activity separately. However, it raises the important question of the relative importance of different regulatory systems: hormones and local regulatory molecules, and geometric influences on bone formation. The geometry of a BMU

<sup>1</sup>Corresponding author. Email address:  
pascal.buenzli@uwa.edu.au

may influence bone refilling at several levels and for different reasons. It may influence osteoblast secretory activity via osteocyte regulation as in Martin's hypothesis [21], and it may influence changes in the surface density of osteoblasts due to the evolving bone surface area of the refilling BMU cavity [20, 38]. These geometric influences constitute inevitable effects that are important to estimate so as to deduce the precise contributions of other regulatory mechanisms, such as the hormonal and local biochemical regulation of cells.

The specific influence of geometry on osteoblast development and osteoblast level of activity is hard to determine *in vivo* due to the experimental difficulty of controlling this geometry. Geometric changes during new bone formation are the result of the (geometry-dependent) collective dynamics of osteoblast activity, and also depend on the geometry of the bone substrate previously shaped by osteoclasts. In Ref. [23], the local curvature of the substrate on which new bone is formed was shown to influence matrix apposition rate in an *in-vitro* system, but the respective contributions of osteoblast population and osteoblast level of activity was not investigated. The difference between matrix apposition rate in cortical BMUs and trabecular BMUs also suggests that geometry plays an important role during bone apposition [1, 20, 21]. The experimental challenges associated with the study of geometric influences on bone cell development and on cell secretory activity *in vivo* emphasise the need for accurate computational models to help understand the specific contribution of geometry versus other regulatory systems, and thereby help interpret experimental data.

Insights into how osteoblast secretory activity is regulated in a BMU could be gained by estimating secretory activity levels at different phases of the refilling process in the BMU, *i.e.*, at different locations in the closing cone of the progressing BMU. The local secretory activity of osteoblasts can be deduced from the local measurement of both the bone formation rate and the density of cells. Tetracycline double labelling and histomorphometric analyses enable the determination of geometric properties such as the radius of the BMU cavity  $R$  and the so-called 'matrix apposition rate'  $\left| \frac{\partial R}{\partial t} \right|$  (*i.e.*, the thickness of the new bone layer deposited per unit time, or speed of linear deposition) [1, 16]. The distribution of cells along a BMU [24] can be revealed experimentally by serial sectioning and histomorphometry [18, 25], or confocal microscopy [26]. However to our knowledge, this data have not been reported in the literature [20]. Marotti *et al.* [18] performed serial sections of BMUs, but a quantitative analysis is only presented for three cross-sectional slices.

In this paper, we therefore follow a different approach and take the information of osteoblast distribution along the BMU that is predicted using a mathematical model of cell development in a cortical BMU. The model is based on biochemical regulation of bone cell developments and extends our previous model [24] by including important influences on the density of osteoblasts in the BMU, namely, a geometrical effect of cavity shrinkage on the density of osteoblasts, an osteoblast-to-osteocyte transition (that likewise depends on the geometry) and an osteoblast-to-bone lining cell transition at the end of the refilling process. The model is calibrated for osteoclast, osteoblast, and precursor cell numbers in the BMU [2, 27], and for osteoblast surface densities at three radii

of the BMU cavity [18]. The experimental values of osteoblast secretory activity  $k_{\text{form}}$  (volume of osteoid secreted per cell per unit time) obtained by Marotti *et al.* [18] at three different radii are extrapolated into a functional dependence of  $k_{\text{form}}(x, t)$  upon the current radius  $R(x, t)$  of the BMU cavity.

The prediction of our mathematical model for the geometric refilling rate are then compared with experimental data from tetracycline double labelling experiments [16]. This comparison enables us to analyse data obtained from several BMUs at a single snapshot in time [16] in terms of the simulated spatio-temporal dynamics of a single BMU. In particular, our model suggests that tetracycline double labelling data provides an incomplete account of the whole refilling process in a BMU, that does not represent the start and the end of refilling. Importantly, we find that a large variability in experimental data may arise if measurements are performed on BMUs at different stages of their lifetime, such as initiation stage, progression stage, and termination stage (an information that is usually not known in histological cross-sections). In particular, the different characteristic times associated with the build-up of the osteoclast population and the osteoblast population within a developing BMU imply that these populations do not reach a quasi-steady state at the same time, despite their biochemical coupling. This is shown to influence the dynamics of refilling at a bone site undergoing remodelling, and so to influence tetracycline data collected at this site.

Below, we begin by providing a general derivation of the relationship between cell number, level of secretory activity, and geometric refilling rate. This derivation applies to osteons of any shape and may thereby be useful for experimental studies of the kinetics of regulation of bone balance in BMUs (see the Conclusions, Section 5).

## 2 Methods

### 2.1 Bone refilling dynamics

Active osteoblasts secrete osteoid, a collagen-rich substance that mineralises into new bone. The local production of osteoid depends both on the local number of active osteoblasts and their level of secretory activity. In the following, we consider a transverse cross-sectional slice of thickness  $\delta x$ , at a fixed position  $x$  in bone. The slice corresponds to a region of interest exhibiting the refilling process taking place in the closing cone of the BMU while the BMU progresses through bone along the  $x$  axis (see Figure 1a). We denote by  $S(x, t)$  the surface area of the BMU cavity and by  $P(x, t)$  the perimeter of the BMU cavity at time  $t$  in this cross section. To elucidate the relationship between BMU refilling rate, number of active osteoblasts, and individual osteoid secretion rate, we assume that

1. The osteoid secretion rate  $k_{\text{form},i}(t)$  (in volume per unit time) at time  $t$  of a single active osteoblast  $i$  in the cross-sectional slice only depends on that osteoblast's microenvironment (such as the presence of nutrients, hormones and regulatory molecules [2, 3, 28], and the local curvature of the cavity [20, 23]). This microenvironment is assumed to consist of influences from within the cross-sectional slice at position  $x$ , and so  $k_{\text{form},i}(t) = k_{\text{form}}(x, t)$ .

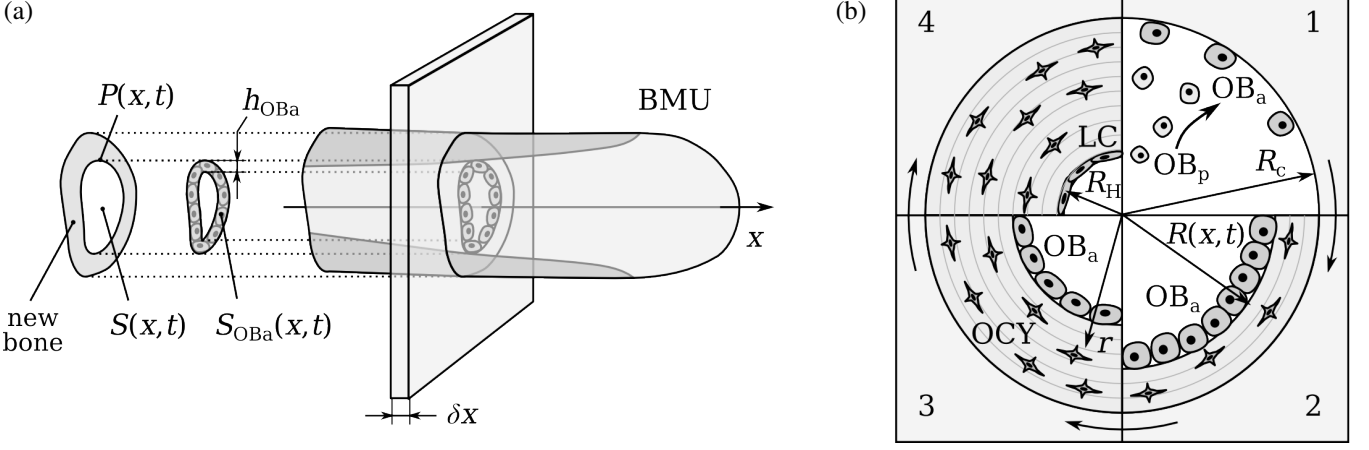


**Figure 1** – (a) A slice (of thickness  $\delta x$ ) at position  $x$  along the BMU showing the surface area of newly-formed bone, the surface area of the cavity  $S(x,t)$  and its perimeter  $P(x,t)$ , and the surface area of the ring-like region containing active osteoblasts  $S_{OBa}(x,t)$ . (b) Four stages of the formation phase of the BMU: 1. Onset of formation: differentiation of pre-osteoblasts ( $OB_p$ ) into active osteoblasts ( $OB_a$ ); cavity radius equal to the cement line radius  $R_c$ ; 2. Early stage of formation, showing that some osteoblasts have become osteocytes (OCY) embedded in the bone matrix; cavity radius  $R(x,t)$ ; 3. Mid stage of formation;  $r$  denotes a radial coordinate; 4. End of formation: the active osteoblasts have become bone lining cells (LC) and the cavity radius is the Haversian canal radius  $R_H$ .

2. Osteoid is not transported into the cross-sectional slice or away from it: an increase in osteoid volume within the slice is only due to the active osteoblasts present there, and serves entirely to refill the BMU cavity in this slice (Figure 1). This hypothesis is supported by the observation that osteoblasts do not move significantly along the longitudinal axis of the BMU while they deposit osteoid [1, 2, 24, 29, 30].

The total volume of osteoid produced per unit time in the slice is given by  $\sum_i k_{form,i}(t)$ , where  $i = 1, 2, \dots$  runs over the collection of active osteoblasts in the slice. This newly-formed bone progressively closes the BMU cavity, of surface area  $S(x,t)$ , according to:

$$\frac{\partial}{\partial t} S(x,t) \delta x = - \sum_{i=1,2,\dots} k_{form,i}(t) = -k_{form}(x,t) \delta N_{OBa}(x,t), \quad (1)$$

where  $\delta N_{OBa}(x,t)$  is the number of active osteoblasts in the slice at  $x$ . Introducing the surface density of active osteoblasts,

$$\rho_{OBa}(x,t) = \frac{\delta N_{OBa}(x,t)}{\delta x P(x,t)}, \quad (2)$$

Eq. (1) becomes:

$$\frac{\partial}{\partial t} S(x,t) = -k_{form}(x,t) \rho_{OBa}(x,t) P(x,t). \quad (3)$$

The specialisation of Eq. (3) to a rotation-symmetric cortical BMU of cavity radius  $R(x,t)$  gives, substituting  $S(x,t) = \pi R(x,t)^2$  and  $P(x,t) = 2\pi R(x,t)$ :

$$\frac{\partial}{\partial t} R(x,t) = -k_{form}(x,t) \rho_{OBa}(x,t), \quad (4)$$

where  $|\frac{\partial}{\partial t} R(x,t)|$  is the so-called *matrix apposition rate* [1, 31]. Interestingly, the BMU cavity radius  $R(x,t)$  does not appear *explicitly* in the right hand side of Eq. (4), in contrast to the presence of a geometrical property of the cavity (the perimeter  $P$ ) in the right hand side of Eq. (3). In fact, it can be shown that the matrix apposition rate  $v_{form}^\perp$  at a position  $r$  of the bone surface, defined by the thickness of newly-formed bone deposited per unit time, is always given by

$$v_{form}^\perp(r,t) = k_{form}(r,t) \rho_{OBa}(r,t), \quad (5)$$

irrespective of the geometry of the bone surface (such as the local curvature) and irrespective of the direction of movement of the osteoblasts during the deposition (see Appendix A).<sup>1</sup> The occurrence of an explicit geometric factor of the BMU cavity in the right hand side of Eq. (3) reflects the fact that Eq. (3) corresponds to the average of the local refilling dynamics equation (5) over the cross-sectional slice (see Appendix A). In contrast to Eq. (4), Eq. (3) applies to arbitrarily-shaped cortical BMUs, as well as trabecular BMUs and formative bone modelling for appropriate definitions of  $S$  and  $P$ . We note here that the local law (5) applies in fact more generally to any cell-driven biosynthetic or catalytic process occurring from the surface of a pre-existing substrate, in which the synthesised or catalysed material does not diffuse.<sup>2</sup>

The refilling dynamics (3), (4), and (5) express the general relationship between geometric refilling rate ( $\frac{\partial}{\partial t} S$ ,  $\frac{\partial}{\partial t} R$ , or  $v_{form}^\perp$ ), osteoblast population<sup>3</sup> ( $\rho_{OBa}$ ) and osteoblast activity ( $k_{form}$ ). These equations can be used to determine one of these quantities from the knowledge of the two others. In particular, insights into how osteoblast activity  $k_{form}$  is regulated in a BMU can be gained by determining  $k_{form}$  at different phases of BMU refilling, for example by determining its variation along the length of the BMU [18]. Unfortunately, this data has rarely been measured [20].

*Implicit* dependences upon geometrical properties of the BMU cavity in both osteoid secretion rate  $k_{form}$  and osteoblast density  $\rho_{OBa}$  may of course be present. In fact, phenomenological relationships between matrix apposition rate and the BMU cavity radius in cortical bone [11–15, 21], or between matrix apposition rate and the local curvature in the *in-vitro* systems of Ref. [23] emphasise such implicit dependences.

<sup>1</sup>The matrix apposition rate is denoted here by  $v_{form}^\perp$  as it corresponds to the normal component of the velocity of the bone surface, see Appendix A.

<sup>2</sup>For example, Eq. (5) applies to bone resorption if replacing osteoblast properties by osteoclast properties. However in this case, the spatial integration of the local law (5) does not retrieve an equation of the form (3) due to osteoclast movement along the  $x$  axis (see also Discussion, Section 4).

<sup>3</sup>Provided that there is no gap between adjacent osteoblasts, the surface density of active osteoblasts is the inverse of their so-called ‘secretory territory’, *i.e.*, their contact area with the bone surface, which is measured in Refs [17, 18].

In this paper, we will investigate more particularly the implicit dependence of  $\rho_{\text{OB}_a}$  upon the BMU cavity radius  $R(x, t)$  in cortical BMUs by modelling the interactions between osteoblasts and the bone surface on the cellular level. The implicit dependence of  $k_{\text{form}}$  upon  $R(x, t)$  will be extrapolated from experimental data from Ref. [18].

## 2.2 Computational model for osteoblast distribution in the BMU

The surface density of osteoblasts depends both on biochemical processes modifying the number of osteoblasts in the slice, and on the local bone surface area, which also evolves in time. In the following, we restrict to rotation-symmetric cortical BMUs and the refilling dynamics described by Eq. (4). The BMU cavity radius is therefore the only geometrical parameter to consider. This restriction enables a more direct comparison with data derived from tetracycline double labelling experiments, in which only BMU cavity radii are reported (usually averaged over four directions in each cross-sectional BMU, see e.g. [9, 11]).

There is an increasing interest in the development of mathematical and computational models of cell populations in bone remodelling, due to the complexity of the spatio-temporal dynamics of cell–cell and cell–bone interactions. In recent years, several teams of researchers have developed such mathematical models, either focused on the tissue scale [32–37] or on the scale of a single BMU [24, 38–43]. To our knowledge, the only previous mathematical model investigating the refilling process of a BMU in some detail is that of Ref. [38]. However, in Ref. [38], the resorption process and the start of the refilling process are not modelled. The refilling process starts with an assumed initial population of active osteoblasts.

The present work is based on our previous mathematical model of osteoclast and osteoblast development in a cortical BMU in one spatial dimension (the BMU longitudinal axis). In our model [24], biochemical coupling between osteoclasts and osteoblasts and migration properties of these cells were estimated and led to the emergence of a stable moving structure (the BMU). The spatial distributions of cells along the longitudinal axis  $x$  were segregated, with osteoclasts towards the front of the BMU and osteoblasts towards the back of the BMU. In the model [24], active osteoblasts derived from pre-osteoblasts ( $\text{OB}_p$ ), which themselves derived from mesenchymal stem cells, at rates depending on the presence of transforming growth factor  $\beta$  ( $\text{TGF}\beta$ ). Active osteoblasts were assumed to be eliminated from the ‘active’ cell pool at a constant rate, combining osteoblast-to-osteocyte transition, osteoblast-to-lining cell transition and osteoblast apoptosis in a single parameter. Here, we extend the model [24] by calculating the evolution of the cavity radius according to Eq. (4) and by including explicitly the following influences on the density of active osteoblasts:

1. *Geometric influence of surface availability:* cavity shrinkage due to refilling reduces the surface area of the bone interface and confines osteoblasts onto a smaller surface (or equivalently, into a smaller volume); this tends to increase osteoblast density;
2. *Osteoblast-to-osteocyte transition:* a fraction of active

osteoblasts becomes trapped in new bone matrix to become osteocytes. This tends to decrease osteoblast density;

3. *Osteoblast-to-bone lining cell transition:* the end of the formation phase at the back of the BMU coincides with the terminal differentiation of active osteoblasts into bone lining cells. Osteoid secretion is stopped during this differentiation;
4. *Osteoblast apoptosis:* Due to cavity shrinkage, the volume of bone required to deposit a layer of constant thickness diminishes as refilling proceeds. At the same time, a decreasing number of osteoblasts can access the bone surface and remain active. An increasing number of osteoblasts that are not active, not becoming osteocytes nor bone lining cells therefore arises (i.e., ‘surplus’ osteoblasts) [1, 2]. These osteoblasts are believed to undergo apoptosis (e.g., due to anoikis). Here a constant rate of apoptosis will be assumed for simplicity, however with a value calibrated so as to eliminate these surplus osteoblasts.

Following our previous model [24], the material balance equation for the volumetric density of active osteoblasts ( $\text{OB}_a$ ) in the slice can be written as:

$$\begin{aligned} \frac{\partial}{\partial t} \text{OB}_a(x, t) = & \mathcal{D}_{\text{OB}_p}(x, t) \text{OB}_p(x, t) - A_{\text{OB}_a} \text{OB}_a(x, t) \\ & + G(x, t) \text{OB}_a(x, t) - \sigma_{\text{OCY}}^{\text{prod.}}(x, t). \end{aligned} \quad (6)$$

In Eq. (6), the source term  $\mathcal{D}_{\text{OB}_p} \text{OB}_p$  corresponds to the  $\text{TGF}\beta$ -dependent differentiation rate of pre-osteoblasts ( $\text{OB}_p$ ) into active osteoblasts; the sink term  $-A_{\text{OB}_a} \text{OB}_a$  corresponds to the rate of apoptosis (point 4. above).<sup>4</sup> The last two terms in the right hand side of Eq. (6) are new compared to the model of Ref. [24]. The additional source term  $G \text{OB}_a$  describes the tendency of cavity shrinkage to increase the density (point 1. above). The additional sink term  $-\sigma_{\text{OCY}}^{\text{prod.}}$  describes the osteoblast-to-osteocyte transition (point 2. above). The precise form of these terms (in particular, their dependence on the cavity radius  $R(x, t)$ ) is presented in detail in Appendix A. Details on how the transition of osteoblasts into bone lining cells is included in the model (point 3. above) are presented below.

**Surface density and volumetric density of active osteoblasts.** Biochemical processes of cell development are best described in terms of volumetric concentrations of signalling molecules and volumetric density of cells. Indeed, biochemical reaction rates depend on the probability of encounter of the interacting biochemical compounds. This probability depends in turn on how closely packed the compounds are, and so, on their local concentration or density (number per unit volume) [44].<sup>5</sup>

<sup>4</sup>Whilst the sink term  $-A_{\text{OB}_a} \text{OB}_a$  has the same form as in Ref. [24], it now solely represents apoptosis of active osteoblasts, and not other depletion pathways of the pool of active osteoblasts (such as the osteoblast-to-osteocyte and osteoblast-to-bone lining cell transitions).

<sup>5</sup>To align with common practice, we use the terminology ‘concentration’ for signalling molecules and ‘density’ for cells, even though both terminologies refer to the same units (i.e., number per unit volume).



**Table 1** – Osteoid secretion rate vs BMU cavity radius (in dogs)

$R^{\text{dog}} [\mu\text{m}]$	$k_{\text{form}}^{\text{dog}} [\mu\text{m}^3/\text{day}]$
15	0
17	90
31	103
65	180

The material-balance equation (6) for active osteoblasts involves biochemical reactions depending on volumetric cell densities (e.g.,  $\text{OB}_p$ ) and molecule concentrations (e.g.,  $\text{TGF}\beta$ ) [24]. This equation is therefore written for the volumetric density of active osteoblasts,  $\text{OB}_a$ . However, active osteoblasts in a BMU are only found on the bone surface and so the refilling dynamics described by Eqs (3)–(5) involves their surface density  $\rho_{\text{OB}_a}$ . To relate the volumetric density  $\text{OB}_a$  to the surface density  $\rho_{\text{OB}_a}$  such that  $\text{OB}_a$  conveys the information of how densely packed active osteoblasts are on the bone surface, we use the fact that active osteoblasts in a BMU form a single layer of cells against the cavity walls [18]. In the cross-section, active osteoblasts are confined to an annulus  $S_{\text{OB}_a}$  of width  $h_{\text{OB}_a}$  corresponding to the typical height of an active osteoblast (see Figure 1a). Within this annulus  $S_{\text{OB}_a}$ , active osteoblasts are distributed fairly uniformly, and so  $S_{\text{OB}_a}$  constitutes an appropriate representative surface element to define the volumetric density of active osteoblasts [44, Chap. XIV], i.e.:<sup>6</sup>

$$\text{OB}_a(x, t) = \frac{\delta N_{\text{OB}_a}(x, t)}{\delta x S_{\text{OB}_a}} = \rho_{\text{OB}_a}(x, t) \frac{P(x, t)}{S_{\text{OB}_a}(x, t)}, \quad (7)$$

where Eq. (2) has been used for the second equality. In a rotation-symmetric BMU,  $P(x, t) = 2\pi R(x, t)$  and

$$S_{\text{OB}_a}(x, t) = \pi [R(x, t)^2 - (R(x, t) - h_{\text{OB}_a})^2]. \quad (8)$$

The mathematical relationship between osteoblast surface density and volumetric density can thus be written as:

$$\rho_{\text{OB}_a}(x, t) = \text{OB}_a(x, t) h_{\text{OB}_a} \left( 1 - \frac{h_{\text{OB}_a}}{2R(x, t)} \right). \quad (9)$$

We note that in the above relationship between  $\rho_{\text{OB}_a}$  and  $\text{OB}_a$ , the geometric factor  $(1 - \frac{h_{\text{OB}_a}}{2R(x, t)})$  accounts for the nonzero curvature  $1/R$  of the cavity (a flat surface has zero curvature, corresponding to the limiting case  $R \rightarrow \infty$ ). Substituting Eq. (9) into Eq. (4) gives:

$$\frac{\partial}{\partial t} R(x, t) = -k_{\text{form}}(x, t) \text{OB}_a(x, t) h_{\text{OB}_a} \left( 1 - \frac{h_{\text{OB}_a}}{2R(x, t)} \right). \quad (10)$$

**Osteoblast-to-bone lining cell transition and osteoid secretion rate.** At the end of the formation phase at the back of a BMU, active osteoblasts terminally differentiate into bone lining cells, thus forming a cellular layer on the

<sup>6</sup>Choosing for example the cavity surface area  $S(x, t)$  or the constant osteon cross-section area rather than  $S_{\text{OB}_a}$  to define the local volumetric density  $\text{OB}_a(x, t)$  in Eq. (7), would not make  $\text{OB}_a(x, t)$  represent how densely osteoblasts are packed on the bone surface, an information that is importantly conveyed by the surface density  $\rho_{\text{OB}_a}$  in Eqs (3)–(5). Indeed, active osteoblasts are not distributed uniformly across these other representative surfaces.

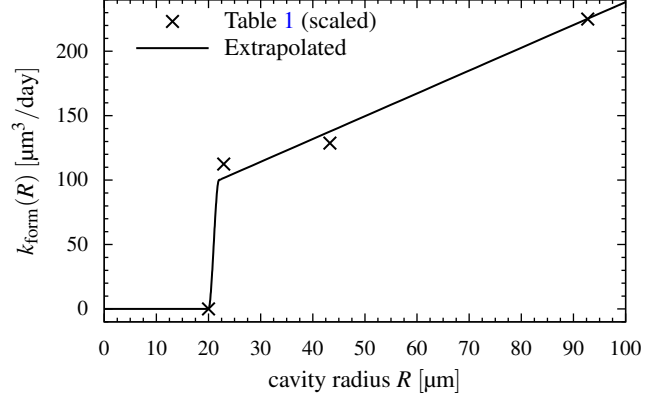


**Figure 2** – Assumed functional relationship  $k_{\text{form}}(R)$  between osteoid secretion rate  $k_{\text{form}}$  and BMU cavity radius  $R$  (solid line). Data points (crosses) are taken from Table 1 and scaled according to Eqs (11), (12).

newly formed bone surface [1, 31]. To account for such a transition in the model while ensuring the spatial exclusion of active osteoblasts and bone lining cells, we assume that active osteoblasts whose osteoid secretion rate  $k_{\text{form}}$  is rapidly dropping become bone lining cells. Osteoid secretion rate by individual osteoblasts varies as refilling proceeds in cortical BMUs [18, 19]. The precise factors that influence osteoid secretion rate are currently not well known. The secretion rate depends on the amount of organelles involved in glycoprotein and protein synthesis, and so is likely to depend on the cell's protoplasmic volume [18, 19, 25]. The observed flattening of osteoblasts as refilling proceeds [1, 18, 19, 31] is associated with a reduction in cell volume and in osteoid secretion rate [18, 19, 25].

To account for the variation of osteoid secretion rate during the refilling process in our model, we assume that  $k_{\text{form}}$  depends on the current radius of the cavity:  $k_{\text{form}}(x, t) = k_{\text{form}}(R(x, t))$ , with  $k_{\text{form}}(R_H) = 0$ , where  $R_H$  is the Haversian canal radius at which osteoblasts have become (non-synthesising) bone lining cells (see Figure 1b). Marotti *et al.* [18] have reported values for the osteoid secretion rate at three different radii in canine cortical BMUs. We add to this data a zero secretion rate at a Haversian canal radius  $R_H^{\text{dog}} \approx 15 \mu\text{m}$ , corresponding to the average Haversian canal radius in dogs [31] (see Table 1). The canine data of Table 1 is then used to generate pseudo-human data by appropriate scalings as explained in the next paragraph. We finally interpolate this scaled data by a continuous piecewise polynomial curve  $k_{\text{form}}(R)$  that has a sharp stepwise increase from  $R = R_H = 20 \mu\text{m}$  to  $R = 22 \mu\text{m}$ , and a linear slope for  $R \geq 22 \mu\text{m}$ , as depicted in Figure 2.

### Scaling data from animal models to humans.

Tetracycline-based bone histomorphometry has been performed in several species, such as humans [45, 46], sheep [16], dogs [11, 13–15, 18], and cats [12]. However, some of the quantitative measurements of BMU-related quantities useful to define, calibrate and validate our model are derived from animal models, such as cell surface densities and osteoid secretion rates at different BMU cavity radii [18], total cell numbers [27, 31], and tetracycline double labelling radii [16]. To utilize such data consistently with human data in the calibration of the model to a human cortical BMU, we scale some of this animal data to (pseudo-)human

values according to known (or suspected) cross-species differences [47].

In particular, we scale the radius data  $R^{\text{dog}}$  from Table 1 to (pseudo-)human radius data  $R$  by assuming a linear relationship  $R = R(R^{\text{dog}})$  such that  $R(R_H^{\text{dog}}) = R_H$  and  $R(R_c^{\text{dog}}) = R_c$ , where  $R_H^{\text{dog}} \approx 15 \mu\text{m}$ ,  $R_H \approx 20 \mu\text{m}$  are typical Haversian canal radii in dogs and humans, and  $R_c^{\text{dog}} \approx 70 \mu\text{m}$ ,  $R_c \approx 100 \mu\text{m}$  are typical cement line radii in dogs and humans, respectively [1, 31, 47] (see Figure 1b).<sup>7</sup> This gives:

$$R(R^{\text{dog}}) = R_H + \frac{R_c - R_H}{R_c^{\text{dog}} - R_H^{\text{dog}}}(R^{\text{dog}} - R_H^{\text{dog}}). \quad (11)$$

We also scale the osteoid secretion rates  $k_{\text{form}}^{\text{dog}}$  of Table 1 estimated by Marotti *et al.* [18], by a factor  $\alpha_{k_{\text{form}}} = 1.25$  to account for higher secretion rates in humans [38], *i.e.*:

$$k_{\text{form}} = \alpha_{k_{\text{form}}} k_{\text{form}}^{\text{dog}}. \quad (12)$$

The specific numerical value of the factor  $\alpha_{k_{\text{form}}}$  is chosen so as to reduce the total number of active osteoblasts in the BMU (see Results and Discussion, Sections 3,4). The scaled radius and osteoid secretion rate data of Table 1 are shown in Figure 2 (crosses).<sup>8</sup>

Scalings are also applied to the data of Table 2 reporting canine osteoblast surface densities  $\rho_{\text{OB}_a}^{\text{dog}}$  at three BMU cavity radii (see Results, Section 3). The radii  $R^{\text{dog}}$  are scaled to correspond to human average BMUs as in Eq. (11). The osteoblast surface densities  $\rho_{\text{OB}_a}^{\text{dog}}$  are scaled to pseudo-human data as  $\rho_{\text{OB}_a} = \alpha_{\rho_{\text{OB}_a}}^{-1} \rho_{\text{OB}_a}^{\text{dog}}$ . The choice of the scaling factor  $\alpha_{\rho_{\text{OB}_a}}^{-1} = 0.8$  is motivated by the corresponding scaling factor  $\alpha_{k_{\text{form}}} = 1.25$  performed on  $k_{\text{form}}^{\text{dog}}$ . Indeed, increased osteoid secretion rate is associated with increased cell volume, and thus with a corresponding decrease in cell density [18, 19].

**Governing equations.** The equations describing the evolution of the BMU cavity radius (10) and the evolution of the density of active osteoblasts (6) both govern the dynamics of the refilling towards the back of the BMU. Following our model [24], we define three other state variables of the system: the density of pre-osteoblasts  $\text{OB}_p(x, t)$ , the density of active osteoclasts nuclei  $\text{OC}_a(x, t)$  and the concentration of transforming growth factor  $\beta$ ,  $\text{TGF}\beta(x, t)$ .<sup>9</sup> The balance equations governing these quantities involve several additional signalling molecules, *i.e.* the receptor-activator nuclear factor  $\kappa\text{B}$  system (RANK, RANKL, and OPG) and parathyroid hormone (PTH). However, the dynamics of these additional signalling molecules is fast compared to the characteristic times of cell behaviours [24]. Their balance equations can be taken in a quasi-steady state, enabling the concentration of these signalling molecules to become algebraic expressions of the variables  $\text{OB}_p, \text{OB}_a, \text{OC}_a$  and  $\text{TGF}\beta$ . The material balance equations governing the evolution of all the variables are presented in Appendix A, see Eqs (19)–(30).

<sup>7</sup>In Ref. [31], the average cement line radius in dogs is reported to be  $R_c^{\text{dog}} \approx 60 \mu\text{m}$ . In Ref. [47], it is reported to be  $R_c^{\text{dog}} \approx 77 \mu\text{m}$ . Since one of the three BMU cavities in Ref. [18] has a radius  $65 \mu\text{m}$  in the formation phase, we take here  $70 \mu\text{m}$  as the representative cement line radius.

<sup>8</sup>The model of Polig and Jee [38] suggests that  $\alpha_{k_{\text{form}}}$  may take values from 1.27 to 1.7.

<sup>9</sup>Here and in Ref. [24],  $\text{OC}_a$ s represent mononucleated entities incorporated in a multinucleated active osteoclast. Multinucleated active osteoclasts are composed of about 10 nuclei [27].

**Table 2** – Osteoblast surface density vs BMU cavity radius (in dogs)

$R^{\text{dog}} [\mu\text{m}]$	$\rho_{\text{OB}_a}^{\text{dog}} [\text{mm}^{-2}]$
17	4500
31	8770
65	10000

### 3 Results

**Numerical simulations.** The material balance equations of the average densities of cells and concentrations of signalling molecules (19)–(30) (see Appendix A) together with Eq. (10) form a coupled system of five partial differential equations (PDEs). These PDEs were solved numerically to evolve the system for 150 days from an initial condition with a small, localised population of active osteoclast nuclei ( $\text{OC}_a$ s) and given distributions of  $\text{OB}_a$ s and  $\text{OC}_p$ s concentrated around the (growing) blood vessel extremity of the BMU, as in Ref. [24], see Figure 3a. The initial cavity radius was set to the cement line radius  $R_c$  as only the refilling of the cavity is considered in this paper. We assumed a uniform density of osteocytes  $\text{OCY}_{\text{exp.}}(x, r) \equiv 20000/\text{mm}^3$  [31].

The cells present initially at  $t = 0$  generate a biochemical positive feedback loop, captured in the governing equations: the  $\text{OC}_a$ s free  $\text{TGF}\beta$  from the bone matrix into the microenvironment, which promotes the differentiation of  $\text{OB}_a$ s into  $\text{OB}_p$ s. The ligand RANKL expressed on  $\text{OB}_p$ s promotes in turn the differentiation of  $\text{OC}_p$ s into  $\text{OC}_a$ s, thus enabling the process to be sustained. Further towards the back of the BMU, the concentration of  $\text{TGF}\beta$  drops [24]. This facilitates the differentiation of  $\text{OB}_p$ s into  $\text{OB}_a$ s [2, 3]. At this point, bone formation starts and the cavity refills. After an initial transient during which these processes take place and the population of osteoblasts increases (see Figure 3b), the cell densities reach steady-state distribution profiles progressing forward in bone without changing shape (Figure 3c). Meanwhile, the bone cavity progressively refills (as shown at the bottom of each graphs in Figure 3a–c). The refilling rate is strongly reduced when the cavity radius reaches values close to the ‘target’ Haversian canal radius  $R_H = 20 \mu\text{m}$ . Indeed, close to  $R_H$ , the osteoid secretion rate  $k_{\text{form}}$  drops according to Figure 2. The distribution of  $k_{\text{form}}(R(x, t))$  along the BMU’s longitudinal axis  $x$  at  $t = 150$  days is shown in Figure 3d, along with the locations at which  $k_{\text{form}}$  is 90% and 10% of the step height in Figure 2. These locations suggest the transition of active osteoblasts ( $\text{OB}_a$ s) into bone lining cells (LC) and are represented in Figure 3c by the start and end of the  $\text{OB}_a \rightarrow \text{LC}$  transition arrow. The dot-dashed line in Figure 3c represents the active osteoblast surface density  $\rho_{\text{OB}_a}$  and constant bone lining cell density  $\rho_{\text{LC}} = 2300/\text{mm}^2$  (see right vertical axis) [31]. Surface densities  $\rho_{\text{OB}_a} < 2300/\text{mm}^2$  are shaded as they do not correspond to real active osteoblasts: at these locations, osteoblasts are assumed to have become bone lining cells of constant density no longer secreting osteoid and no longer undergoing apoptosis.

**Calibration of the cell distribution profiles.** Quantitative data on the distribution of cells in cortical BMUs, and/or their total number, is relatively sparse [2, 18, 20, 27, 48]. We calibrated our model such that the cell distribution profiles are in reasonable agreement with the following:

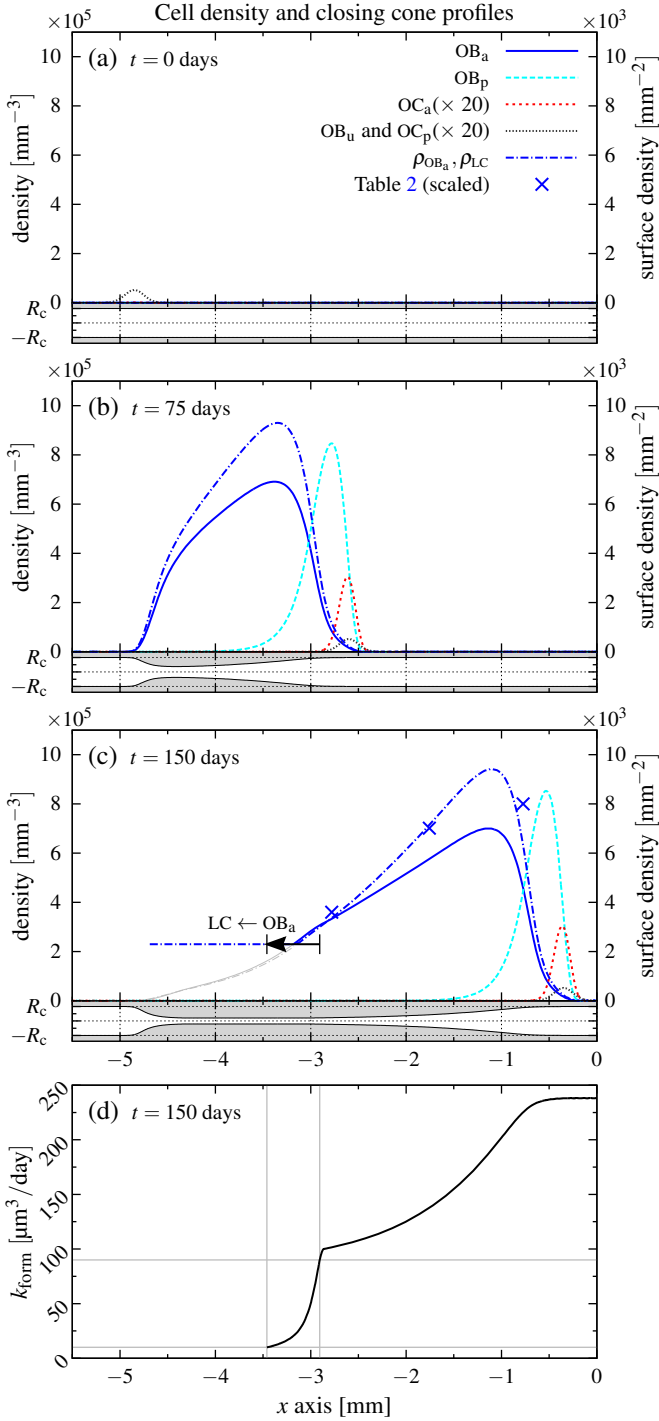


**Figure 3** – (a)–(c) The profiles of cell densities along the BMU’s length (top of each panel) and the corresponding shape of the closing cone (bottom of each panel) are shown at time (a)  $t = 0$  days (initial condition), (b)  $t = 75$  days, and (c)  $t = 150$  days. To ensure that all cell densities are visible,  $OB_u$ ,  $OC_p$ , and  $OC_a$  were multiplied by a factor 20. The active osteoblast surface density  $\rho_{OB_a}$  and bone lining cell surface density  $\rho_{LC}$  are also shown (dot-dashed lines). In (b), individual osteoid secretion rate  $k_{form}$  has not yet dropped enough for  $OB_a$  to differentiate into LC. In (c), an  $OB_a \rightarrow LC$  transition takes place as indicated by the arrow. The arrow starts and ends where  $k_{form}(x, t)$  is 90% and 10% of the “step height” in Figure 2 (see also panel (d)). The crosses in (c) correspond to the experimental data of osteoblast surface density from [18] listed in Table 2, scaled to human values. (d) Profile of osteoid secretion rate  $k_{form}(x, t)$  by active osteoblasts at  $t = 150$  days. The grey lines indicate where  $k_{form}$  is 90% and 10% of the “step height” in Figure 2 ( $OB_a \rightarrow LC$  transition).

- The total number of precursor cells ( $N_{OB_u}, N_{OC_p}$ ) in steady state is about 20;
- The total number of active osteoclast nuclei ( $N_{OC_a}$ ) in steady state is about 100 [27];
- The surface density of active osteoblasts ( $\rho_{OB_a}$ ) in steady state coincides with data reported by Marotti *et al.* [18] at three different cavity radii, whilst the total number of active osteoblasts ( $N_{OB_a}$ ) in steady state is in the range 2000–6000 [27, 31, 38] (see also Discussion, Section 4).

The osteoblast surface densities  $\rho_{OB_a}^{dog}$  reported by Marotti *et al.* [18] in three canine BMU cross-sections are shown in Table 2. The radii  $R^{dog}$  and surface densities  $\rho_{OB_a}$  were scaled to correspond to human average BMUs as mentioned above.

The data on osteoblast surface density at different cavity radii thus rescaled is shown in Figure 3c (crosses) along with the calculated surface density profile  $\rho_{OB_a}$  (blue dot-dashed line).

To calibrate the model against the number of active osteoclast nuclei and precursor cells in the steady-state BMU, the cell densities  $OC_a(x, t)$ ,  $OC_p(x, t)$  and  $OB_u(x, t)$  were integrated over the BMU cavity space  $R(x, t)$  at  $t = 150$  days. An appropriate rescaling of model parameters was thereby determined (see Appendix A) and the model parameters modified according to Eqs (32). With the model parameters listed in Table 3 in Appendix A, we obtained:

$$N_{OC_a} \approx 100, \quad N_{OC_p} \approx 20, \quad N_{OB_u} \approx 20 \quad (13)$$

To calibrate the model against the active osteoblast surface densities at three different cavity radii (Table 2) and against the total number of active osteoblasts, we modified the osteoblast apoptosis rate  $A_{OB_a}$ , the model parameters related to the scaling factor  $\alpha_{OB_a}$ , and the (canine-to-human) scaling factor  $\alpha_{k_{form}}$ . The apoptosis rate  $A_{OB_a}$  influences the spatial rate of decrease of the osteoblast distribution at the back of the BMU [24]. The factor  $\alpha_{OB_a}$  scales the value of the density at each location along the BMU uniformly. The scaling factor  $\alpha_{k_{form}}$  enables to modify the total number of active osteoblasts in the steady state BMU (e.g., increasing  $\alpha_{k_{form}}$  reduces  $N_{OB_a}$ ). The data could be matched very well by modifying these two properties of the distribution profile, as seen in Figure 3c. The total number of pre-osteoblasts (obtained by integrating  $OB_p(x, t)$  over the cavity space) and the total number of active osteoblasts (obtained by integrating the surface density  $\rho_{OB_a}(x, t)$  over the cavity–bone surface) in the steady state BMU (at  $t = 150$  days) were:

$$N_{OB_p} \approx 11\,100, \quad N_{OB_a} \approx 5200. \quad (14)$$

The calibrated model was then validated against three independent sets of experimental data: (i) the density of bone lining cells reached at the end of the formation phase at the back of the BMU; (ii) the length of the formation cone of the BMU; (iii) tetracycling double labelling data.

**Osteoblast-to-bone lining cell transition.** In the model, refilling is strongly reduced when the radius of the cavity reaches the Haversian canal radius  $R_H$  (Figure 2). The surface density of active osteoblasts at which this occurs should be

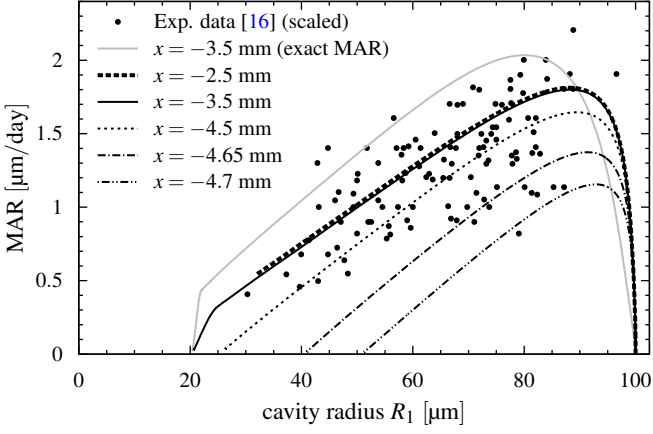


**Figure 4** – Matrix apposition rate versus BMU cavity radius obtained from our model (lines) and from tetracycline experiments (dots). The exact matrix apposition rate  $|\frac{\partial}{\partial t}R(x,t)|$  versus  $R_1 \equiv R(x,t)$  is shown at position  $x = -4$  mm in bone (solid grey line). The approximate matrix apposition rates  $|\frac{R_2 - R_1}{\Delta t}| \equiv |\frac{R(x,t+\Delta t) - R(x,t)}{\Delta t}|$  versus  $R_1 \equiv R(x,t)$  are shown at  $x = -2.5$  mm,  $-4$  mm,  $-4.5$  mm,  $-4.62$ , and  $-4.7$  mm for a fixed interval  $\Delta t = 10$  days. Data points are taken from Ref. [16, Fig. 2] and have been appropriately rescaled to human average BMU sizes (see text).

consistent with experimentally observed surface density of bone lining cells,  $\rho_{LC} \approx 2300/\text{mm}^2$  [31]. We see from Figure 3c that this constraint was satisfied by the model. Indeed, the surface density  $\rho_{OB_a}$  reached the value  $2300/\text{mm}^2$  precisely in the zone in which osteoid secretion rate dropped from 90% to 10% of the step height of  $k_{\text{form}}(R)$  around  $R \approx R_H$  in Figure 2 (see also Figure 3d).

**Length of the formation cone.** Considering the start of the formation cone in Figure 3c to be around  $x \approx -0.5$  mm and the end of the formation cone to correspond to the intersection of the active osteoblast surface density and bone lining cell density at around  $x \approx -3$  mm, the length of the formation cone is about 2.5 mm. This corresponds to values estimated for humans [31].

**Tetracycline double labelling data.** Tetracycline double labelling is an experimental technique enabling the estimation of the matrix apposition rate  $\frac{\partial}{\partial t}R$ . Tetracycline incorporates actively mineralising tissue with a fluorescent dye [1, 9, 31]. Its injection at two successive time points  $t_1$  and  $t_2$  reveals the radii of the BMU cavity at these time points,  $R_1$  and  $R_2$ , from histological slices extracted later [11, 12, 16]. The average matrix apposition rate between  $t_1$  and  $t_2$  can be estimated as  $\text{MAR} \equiv |\frac{R_2 - R_1}{t_2 - t_1}|$ . The data is usually presented in either of two forms: a plot of the data pairs  $(R_1, R_2)$  [12, 15, 16] or a plot of MAR vs either  $R_1$  or  $R_2$  [11, 13, 14, 16]. In both cases a linear relationship is experimentally found.

In Figure 4 we plot the ‘exact’, instantaneous matrix apposition rate  $|\frac{\partial}{\partial t}R(x,t)|$  versus  $R(x,t)$  at  $x = -4$  mm (solid grey line) and the approximate, average matrix apposition rates  $|\frac{R(x,t+\Delta t) - R(x,t)}{\Delta t}|$  versus  $R(x,t)$  obtained in our simulations during the BMU cavity refilling when  $t$  increases from 0 to 150 days. The effect of sampling the radii at various positions  $x$  in bone is shown (black lines), whilst the time interval  $\Delta t = 10$  days (corresponding to the time interval between the tetracycline injections) is kept fixed. These results are compared to experimental data from Metz *et al.* [16]. This

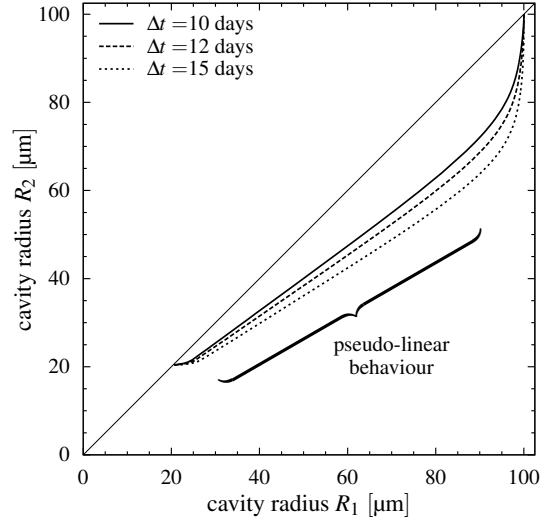


**Figure 5** – Parametric plots of cavity radius pairs  $(R_1, R_2)$  with  $R_1 = R(x,t)$  and  $R_2 = R(x,t + \Delta t)$  obtained from our model at a fixed location in bone ( $x = -4$  mm) when  $t$  evolves from 0 to 150 days. The figure shows the effect of choosing different time intervals  $\Delta t = 10$  days, 12 days, and 15 days (corresponding to typical time intervals between tetracycline injections). The calculated curves intersect with the diagonal at the onset of formation and at completion of formation.

data was collected in sheep and plotted in Ref. [16, Fig. 2] as MAR versus ‘percent unfilled’, *i.e.*, the percent of bone thickness remaining to deposit so as to reach the sheep Haversian canal radius. In Figure 4, we rescaled this ‘percent unfilled’ data to human-sized BMU cavity radii similarly to Eq. (11), such that 100% unfilled corresponds to the cement line radius  $R_c = 100 \mu\text{m}$  and 0% unfilled corresponds to the Haversian canal radius  $R_H = 20 \mu\text{m}$ .

In Figure 5 we plot the trajectory of the radii pairs  $(R_1, R_2) \equiv (R(x,t), R(x,t + \Delta t))$  obtained during the BMU cavity refilling at  $x = -4$  mm when  $t$  increases from 0 to 150 days for various time intervals  $\Delta t$ .

## 4 Discussion

**Cell distribution profiles within the BMU.** As in our previous model [24], the distribution of cell densities along the longitudinal spatial coordinate  $x$  evolves from the initial condition into a stable multicellular travelling-wave-like structure (the BMU) progressing through bone without changing shape, with osteoclasts towards the front of the BMU and osteoblasts towards the back of the BMU (Figure 3a–c). This developing and progressing structure models the initial and quasi-steady phases of a cortical BMU. Its emergence is due to the biochemical coupling between the bone cells and the cells migration properties [24].

The most important difference in the cell distribution profiles of active osteoclasts ( $OC_a$ ) and pre-osteoblasts ( $OB_p$ ) in Figure 3a–c compared with Ref. [24] is a vertical scaling factor due to the calibration of total cell numbers performed here. The overall shape and spatial extension of the distributions of  $OC_a$ s and  $OB_p$ s is otherwise unaltered. By contrast, the shape of the cell distribution profile of active osteoblasts ( $OB_a$ ) is appreciably modified compared to Ref. [24, Fig. 2] due to the addition of the geometric influence of surface availability, osteoblast-to-osteocyte transition, and osteoblast-to-bone lining cell transition in the model. In the current



model, active osteoblasts rise more sharply to their maximum value at the start of formation (near  $x = -0.5$  mm). The decrease of the density of  $OB_a$ s towards the back of the BMU is also more linear in Figure 3c compared to the exponential-like decrease in Ref. [24, Fig. 2], an effect attributable to the tendency of cavity shrinkage to concentrate the density of active osteoblasts. The generation of osteocytes also has an important influence on the decrease of the density of  $OB_a$ s towards the back of the BMU. Indeed, one can observe a small transient reduction in the decrease of  $OB_a$  as a slight “bulge” in the  $OB_a$  density profile near the  $OB_a \rightarrow LC$  transition, where osteocytes stop being generated. This “bulge” is generated despite the density-concentrating effect of cavity shrinkage being reduced at the same time.

The calibration of the active osteoblast surface density  $\rho_{OB_a}$  (dot-dashed blue line) to Marotti *et al.*'s data (crosses) in Figure 3c could be performed very well, in particular thanks to the pseudo-linear decrease of the active osteoblast population towards the back of the BMU obtained with the model. Remarkably, this calibration is consistent with the fact that the cavity is refilled up to the Haversian canal radius  $R_H$  precisely when the surface density  $\rho_{OB_a}$  reaches a bone lining cell surface density of  $2300/\text{mm}^2$  [31]. This is indicated in Figure 3c by the fact that the  $\rho_{OB_a}$  curve intersects the  $OB_a \rightarrow LC$  transition arrow. With poorly-calibrated model parameters the cavity was either under-refilled when  $\rho_{OB_a}$  reached the value  $2300/\text{mm}^2$  or refilled too early, at values of  $\rho_{OB_a}$  larger than  $2300/\text{mm}^2$ , leading to lengths of the closing cone shorter than reported values (see also below).

Osteoblast apoptosis in a BMU is believed to serve to eliminate ‘surplus’ osteoblasts, *i.e.*, osteoblasts that are neither forming bone, nor becoming osteocytes, nor becoming bone lining cells [2]. The rate of osteoblast apoptosis, as a regulatory mechanism of osteoblast number in the BMU closing cone, is thus likely to depend on the phase of the refilling process in the BMU. Indeed, as the cavity shrinks, the number of osteocytes to be generated per unit time decreases and osteoblasts are confined in a smaller volume, resulting in an increase in surplus osteoblasts. Nevertheless, the constant rate of osteoblast apoptosis  $A_{OB_a}$  assumed in our model enabled us to obtain a profile of active osteoblast surface density that accurately matched the experimental measurements of Marotti *et al.* [18] and the bone lining cell density.

**Number of osteoblasts within the BMU** Precise estimates of the total number of active osteoblasts in a BMU are difficult to find in the literature. Numbers in the range 2000–4000 [27], of about 3000 per millimetre of BMU length [38], and up to 6750 [31, Table 6] are reported, probably reflecting cross-sectional and/or cross-species variabilities. Estimates of the local surface density of active osteoblasts  $\rho_{OB_a}$ , or of their secretory territory (corresponding to  $\rho_{OB_a}^{-1}$  if closely-packed) are likely to be more reliable as they are based on local measurements only and do not depend on the length of the closing cone of the BMU. A lower bound of the total number of active osteoblasts  $N_{OB_a}$  can be estimated based on a lower-bound surface density of  $2300/\text{mm}^2$  (surface density of bone lining cells [31]), and a lower-bound cavity–bone surface area given by a linearly changing cavity radius along the formation cone of the BMU (straight lines being the shortest). With a

formation cone length  $L_{\text{form}} \approx 2.5$  mm [31], Haversian canal radius  $R_H \approx 20$   $\mu\text{m}$  and cement line radius  $R_c \approx 100$   $\mu\text{m}$ , this provides the lower bound  $N_{OB_a} \gtrsim 2170$ . Following Parfitt [31], a reasonable upper-bound estimate may be found similarly by assuming a maximum cavity–bone area given by that of a cylinder of radius  $R_c$  and length  $L_{\text{form}}$  and an average surface density  $\rho_{OB_a} \approx 4500/\text{mm}^2$ . This provides the upper bound  $N_{OB_a} \lesssim 7000$ .

The total number of active osteoblasts in the steady-state BMU obtained in our simulations ( $N_{OB_a} \approx 5200$ ) falls well in the above ranges. This total number of active osteoblasts was reached for a scaling of the canine experimental osteoid secretion rates and osteoblast surface densities by the factors  $\alpha_{k_{\text{form}}} = 1.25$  and  $\alpha_{k_{\text{form}}}^{-1} = 0.8$ , respectively, as explained in Methods, Section 2. Without these scalings (for a BMU properly calibrated to the other data), the number of active osteoblasts was about 6600.

As mentioned above, the length of the BMU closing cone is an important factor determining the total number of active osteoblasts. The BMU progression rate in bone,  $v_{\text{BMU}}$ , was found to directly affect this length, and so also the total number of active osteoblasts. Values of  $v_{\text{BMU}}$  in the range 20–40  $\mu\text{m}/\text{day}$  [2, 31] are cited in the literature. The simulations presented here were performed with a BMU progression rate  $v_{\text{BMU}} = 30$   $\mu\text{m}/\text{day}$ . With a BMU progression rate  $v_{\text{BMU}} = 40$   $\mu\text{m}/\text{day}$  and no scaling of the canine data (*i.e.*,  $\alpha_{k_{\text{form}}} = 1$ ), about 8800 active osteoblasts were found in steady-state in a closing cone measuring about 3.5 mm. These results show that a great variability in the total number of active osteoblasts can be achieved within the model with still physiologically reasonable parameter values. Such variability can therefore also be expected in experimental measurements.

Finally, the total number of pre-osteoblasts in the BMU in our simulations ( $N_{OB_p} \approx 11\,100$ ) may seem high, although we are not aware of pre-osteoblast cell counts in BMUs reported in the literature. The high value obtained for  $N_{OB_p}$  compared to  $N_{OB_a}$  is mainly due to the integration of the volumetric density  $OB_p$  across the whole cavity surface  $S(x, t)$ , as opposed to the integration of the density of active osteoblasts near the cavity–bone surface only. We note, however, that the fate of all pre-osteoblasts in the model is to become active osteoblasts at some point of the refilling process, *i.e.* pre-osteoblasts are not assumed to undergo apoptosis. In fact, the number of pre-osteoblasts in a cross-sectional slice of thickness  $\delta x = h_{OB_a} = 15$   $\mu\text{m}$  at a fixed position in bone reaches a maximum value of about 390 near the start of the refilling process, then quickly decreases to zero as pre-osteoblasts become active. This activation process forms a layer of active osteoblasts against the bone surface with precisely the correct surface density, as indicated by the match of the surface density of active osteoblasts  $\rho_{OB_a}$  with the experimental data in Figure 3c. This shows that in terms of cell *densities*, the model is well calibrated, but that *absolute number of cells* derived from the model by integration of the densities may be enticed with large uncertainties, associated with uncertainties (or variabilities) in the domains of integration.

**Shape of the BMU cavity (closing cone).** The BMU cavity represented below each plot in Figure 3a–c has to be interpreted with some care as only the refilling process was

accounted for, not the resorption process. A major difference between the resorption process by active osteoclasts and the formation process by active osteoblasts within a cortical BMU, is that osteoclasts move longitudinally (along  $x$ ) while they resorb bone [31]. This complicates the governing equation for the cavity radius in the cutting cone. Indeed, transport terms along  $x$  due to osteoclast movement are present, which involve spatial derivatives. We note that this complication does not necessarily arise in so-called ‘type II osteons’ (formed by BMUs following a pre-existing Haversian canal [31, 49]) and in trabecular remodelling as in these situations, cellular resorption may be progressing radially only [31].<sup>10</sup>

The local shape of the Haversian canal resulting from the passage of a BMU in a region of bone undergoing remodelling depends on the stage of the BMU’s life that this region of bone experiences. The extent of both resorption and formation depends on whether the BMU was in an initiation phase (early life), in a quasi-steady state (mid life) or in a termination phase (late life). In fact, several levels of quasi-steady states can be defined in a BMU. Indeed, whilst the population of certain cell types may have reached a quasi-steady-state within the BMU, the population of other cell types may still be developing. Due to the longer lifespan of osteoblasts compared to osteoclasts, we observe that osteoclast cell densities reach a steady state earlier in the BMU’s life than osteoblast cell densities. For example, in Figure 3b (at  $t = 75$  days), the density of active osteoclasts ( $OC_a$ ) has already reached a quasi-steady state but not the density of  $OB_a$ s near the back of the BMU. It is therefore likely that regions of bone in a BMU’s path experience the full extent of the BMU’s resorption but are only partially refilled due to the density of osteoblasts having not fully evolved to a steady state at this location. This situation is mimicked in our simulations by the refilling process occurring near  $x = -4.65$  mm in Figure 3a–c, where a large cavity generated by a mature BMU osteoclastic front is only partially refilled.<sup>11</sup> This creates a local enlargement of the Haversian canal that may be contributing to local spatial nonuniformities observed in Haversian canal sizes [43, 50, 51]. The observation of such local enlargements may be useful for the determination of the location of a BMU’s birth from micro-CT scans exhibiting the Haversian pore system [51].

**Comparison with tetracycline double labelling data.** The calibration of the active osteoblast surface density  $\rho_{OB_a}$  (dashed blue line) to Marotti *et al.*’s data (crosses) in Figure 3c also provides a remarkable consistency between the BMU cavity refilling dynamics of the model and experimental tetracycline double labelling data (see Figure 4). However, the prediction of the model and the experimental data need to be compared with some care. The instantaneous matrix apposition rate  $|\frac{\partial}{\partial t}R(x,t)|$  (Figure 4, solid grey line) differs

significantly from its approximation  $|\frac{R(x,t+\Delta t)-R(x,t)}{\Delta t}|$  (solid black lines and dots). Experimentally, relatively large time intervals between the tetracycline injections ( $\Delta t \approx 7-12$  days) are usually prescribed so as to clearly distinguish both labels in the histological sections [10]. However, mathematically  $|\frac{\partial}{\partial t}R(x,t)|$  is defined in a continuous limit in which  $\Delta t \rightarrow 0$ . In fact, the experimental matrix apposition rate above represents a better estimate of  $|\frac{\partial}{\partial t}R(x,t+\frac{\Delta t}{2})|$  rather than  $|\frac{\partial}{\partial t}R(x,t)|$ , but it is nevertheless usually compared with the radius of the cavity at time  $t$ .

Experimental measurements of label radii are often performed on a collection of different osteons, rather than on serial sections of a single osteon [11, 12, 16]. Having observed great cross-sectional variations of cement line radii and Haversian canal radii, the authors of Ref. [16] have presented MAR versus the percentage of unfilled bone to normalise the data from different osteons. We therefore took this normalised data to compare with the result of our simulations performed on a single BMU.

The numerical results in Figure 4 (lines) clearly exhibit the start and the end of the formation phase, at which  $MAR = 0$ . The sharp rise of the active osteoblast population at the start of formation is reflected by a sharp increase of MAR near the cement line radius  $R_c = 100$   $\mu\text{m}$ . Matrix apposition rate then steadily decreases as refilling proceeds and cavity radius shrinks. The Haversian canal radius eventually reached is given by the point at which  $MAR = 0$ . Because osteoid secretion rate is assumed to decrease sharply when the cavity radius approaches  $R_H = 20$   $\mu\text{m}$ , a sharp fall of MAR near  $R_H$  is also observed. The rise of MAR at the start of the formation and the fall of MAR at the end of the formation are not reflected in the experimental data. This strongly suggests that both the start and the end of the formation phase may occur rapidly, perhaps as a synchronised event amongst all the osteoblasts. A synchronised halt of formation may allow the BMU cavity to reach a target size more consistently. One potential mechanism is that osteoblasts sense the proximity of the blood vessel or other localised components, as suggested *e.g.* in Ref. [20].

Interestingly, for the most part, the numerical curve MAR versus  $R_1$  exhibits a pseudo-linear character. This pseudo-linear character is consistent with the experimental literature, in which such apparent linear relationship is often fitted by lines passing at or near the origin  $(R, MAR) = (0, 0)$  or is written as the phenomenological law:  $MAR = \frac{\partial}{\partial t}R = CR$  [11, 12, 14, 15, 38], despite MAR being normally zero at the Haversian canal radius  $R_H$  (not at  $R = 0$ ). This gives additional support to the suggestion that active osteoblasts may stop bone formation in unison. Indeed, the continuation of the pseudo-linear part of the solid black curve in Figure 4 reaches a point near the origin, while the end of formation clearly corresponds to the point  $(R, MAR) = (R_H, 0)$ . This thus suggests that near the end of formation, the curve  $MAR(R)$  falls abruptly to the point  $(R_H, 0)$ , as in Figure 4. Similar remarks apply to the  $(R_1, R_2)$  data in Figure 5. In Figure 5, the start and end of formation correspond to the points  $(R_c, R_c)$  and  $(R_H, R_H)$ , respectively. A pseudo-linear behaviour is also observed for a significant part of the numerical curves, whose extrapolation may pass at or near the origin  $(R_1, R_2) = (0, 0)$ .

In spite of the normalisation of the data performed by

<sup>10</sup>For example, in the mathematical models of trabecular BMUs of Refs [39, 40, 42], only radial resorption is considered.

<sup>11</sup>In the simulation corresponding to Figure 3a–c, the density of osteoclasts quickly increases from almost zero to stabilise to a quasi-steady state at around 7–8 days (data not shown). All the bone in the BMU’s path located at  $x \gtrsim -4.65$  mm therefore experiences the full extent of the resorption phase of the BMU, where  $-4.65$  mm corresponds to the location of BMU origination  $x_0 = -4.85$  mm plus the distance travelled by the BMU during 7 days (about 200  $\mu\text{m}$ ). In contrast, the density of osteoblasts takes about 50 days from the BMU’s origination to increase to its maximum value.

Metz *et al.* [16] to reduce cross-sectional variability and thereby approximate a ‘typical’ osteon, another source of variability in the data is manifestly present. Our numerical model suggests that the stage of the BMU’s life at which the data is collected may be an important contributor to such variability. In Figure 4, we show numerical curves obtained at different locations  $x$  in the bone. Since the BMU is created at time  $t = 0$  near  $x = -4.85$  mm, different locations  $x$  in bone see the passage of the BMU at different stages of its lifetime. Values of  $x \approx -4.65$  mm experience the passage of the BMU in an initiation phase with nonsteady cell densities (in particular a non-fully-developed osteoblast population, see footnote 11). Larger values of  $x \gtrsim -3.5$  mm experience the passage of the BMU in which cell profiles have all reached a quasi-steady state.<sup>12</sup> A possible explanation of the variability of the experimental data [16] reproduced in Figure 4 is therefore that the tetracycline data may have been collected from BMUs at different stages of their lifetime. This hypothesis is consistent with the observation of Metz *et al.* [16] that measured cement line radii exhibited great variability. If so, the frequency of data points lying on curves obtained from different stages of the lifetime of BMUs in Figure 4 may enable an experimental determination of the relative duration of these stages of a BMU’s lifetime, much in the same way as the frequency of BMUs seen in a resorption or formation phase in histological cross sections enable the experimental determination of the duration of resorption and formation phases in BMUs [1].

Choosing different time intervals between the tetracycline injections also has a marked effect in the curves MAR versus  $R_1$  or  $R_2$  versus  $R_1$ . This effect is shown in Figure 5. However,  $\Delta t$  is experimentally well controlled. By contrast, the knowledge of whether the BMU that formed new bone at the location of the cross-section at  $x$  was in an initiation stage or in a quasi-steady state is not straightforward to determine.

**Osteoid secretion rate.** We assumed in our model that the osteoid secretion rate  $k_{\text{form}}$  was determined by the current BMU cavity radius  $R$  (see Figure 2). The experimental correlation between MAR and cavity radius  $R$  does not necessarily imply a causal relationship between  $R$  and  $k_{\text{form}}$ . However, it is possible that the local curvature of the bone substrate (equal to  $1/R$  in a rotation-symmetric cortical BMU) influences osteoblast membrane stress [20], integrin connections between neighbouring osteoblasts, and/or the transmission of osteocytic signals [21, 22]. This may influence in turn the osteoblasts’ shape, size, and osteoid secretion rate [18, 23]. A biological advantage of having the osteoid secretion rate  $k_{\text{form}}$  effectively regulated by  $R$  is that BMU refilling becomes self-regulated: formation stops when refilling is complete. However, completion of refilling also requires that the population of active osteoblasts can be sustained long enough. We note that ‘over-refilling’ in cortical BMUs is not possible when associated with a new Haversian canal (‘type I osteons’) [1] and only possible to a certain extent when associated with a pre-existing Haversian canal (‘type II osteons’) [31, 49].

<sup>12</sup>An indication that the location  $x = -4$  mm experiences the passage of steady-state profiles is given by the overlap of the curve obtained at  $x = -4$  mm and that obtained at  $x = -2.5$  mm in Figure 4. We note that the bone located at  $x = -2.5$  mm does not experience the passage of the back of the BMU by  $t = 150$  days. This explains why the curve obtained at  $x = -2.5$  mm is incomplete compared to that obtained at  $x = -4$  mm.

Indeed, in the latter case, the Haversian canal of the old osteon may become smaller in the new osteon, corresponding to a net bone gain.

The scarcity of experimental data on the osteoid secretion rate of individual osteoblasts in bone remodelling is perhaps surprising given that it may be easily determined by means of Eqs (3)–(5), combined with measurements of osteoblast surface densities (or secretory territory [17]) and rates of cavity changes. The advantage of Eq. (5) is that it holds locally. By measuring the secretory territory of an osteoblast and the (perpendicular) distance between two tetracycline labels at the osteoblast’s position, Eq. (5) enables in principle the investigation of nonuniformities in the osteoid secretion rate  $k_{\text{form}}$  going down to individual osteoblasts within the same BMU cross-section. The advantage of Eq. (3) is that it directly provides an osteoid secretion rate averaged over the osteoblasts in the cross-section. By measuring the surface area and perimeter of the BMU cavity [9], Eq. (3) enables the determination of osteoid secretion rates from irregular osteons, in contrast with Eq. (4).

## 5 Conclusions

We have developed a mathematical model of cell development within a cortical BMU including several influences of the BMU cavity on the density of active osteoblasts, either explicitly (*e.g.*, via surface availability) or implicitly (*e.g.*, via osteoblast-to-osteocyte transition). This model was calibrated against experimental data on total cell numbers and osteoblast surface densities at three different BMU cavity radii. The comparison of the calibrated model with tetracycline double labelling data revealed in particular the following points:

- Tetracycline data measured on histological cross-sections of bone do not exhibit the start and the end of the refilling phase of BMUs. The build up of the population of active osteoblasts at the onset of refilling and their transition to non-synthesising bone lining cells at completion of refilling should be associated with low and nearly zero matrix apposition rates, respectively. The fact that this is not observed may indicate that in a BMU, the refilling process starts and ends rapidly, as suggested by our model. We note, however, that large and irregular Haversian canals, likely to be in an early stage of refilling, are often discarded from tetracycline analyses [12]. This difficulty could be alleviated by using Eq. (3), valid for any osteon shape, rather than Eq. (4), valid for rotation-symmetric osteons, to analyse the dynamics of BMU refilling.
- The cross-sectional variability remaining in the tetracycline data reported by Metz *et al.* after their normalisation [16, Fig. 2] may be partly due to the fact that the overall refilling dynamics differs in BMUs at different stages of their lifetime (such as initiation stage, progression stage, and termination stage). Due to the short lifespan of osteoclasts compared to osteoblasts, the population of osteoclasts quickly reaches a quasi-steady state early in a BMU’s lifetime, within a few hundreds of micrometres from the BMU’s origination point. In contrast, only regions of bone about 1 mm away from



the BMU's origination point may experience the action of a fully-developed population of active osteoblasts. This may have two additional practical consequences. (i) the location of a BMU's origination may be evidenced by local enlargements of the Haversian pores (due to a local lack of osteoblasts compared to osteoclasts); (ii) it may be possible to determine experimentally the relative duration of the initiation stage and quasi-steady states of a BMU by counting the number of occurrences of BMUs whose tetracycline data falls in specific regions ("bands") in a plot of MAR vs cavity radius  $R$ , as suggested by Figure 4.

A complete quantitative picture of the spatio-temporal dynamics of BMUs based on experimental measurements remains to be elucidated. Whilst matrix apposition rates are often reported in the literature from tetracycline double labelling experiments, these data integrate both osteoblast number and osteoblast secretory activity. Experimental knowledge of osteoid secretion rate per osteoblast is scarce, particularly in relation to a BMU's internal organisation. The determination of cell densities and their distribution along the different phases of the BMU is essential to gain insights into the biochemical regulation of individual cells within the BMU. The latter is important to fully understand how bone formation is regulated in bone remodelling. For example, the biochemical processes leading to the end of the formation phase in a BMU are not clear. Insights into these processes are particularly relevant for our understanding of osteoporosis [5].

## Acknowledgements

Financial support by the Australian Research Council (Project number DP0988427) is gratefully acknowledged.

## Appendix A Model description

In this appendix, we detail some aspects of the model presented in the Methods section (Section 2). The governing equations of all cells and signalling molecules considered in the model are presented, as well as a table listing all the model parameters.

**Bone refilling dynamics.** We first provide a derivation of Eq. (5), locally relating the matrix apposition rate to the number of osteoblasts and their level of secretory activity. An alternative derivation of Eq. (3) by averaging Eq. (5) over the BMU cross-sectional slice is also presented.

The volume of osteoid formed at a position  $r$  of the bone surface during a time increment  $\Delta t$  can be characterised both by the geometric displacement of active osteoblasts during osteoid deposition, and by the amount of osteoid that was produced by the osteoblasts at this location during  $\Delta t$  (see Figure 6). The geometric displacement of an osteoblast at point  $r$  of the bone surface during  $\Delta t$  is given by  $v_{OB_a}(r, t)\Delta t$ , where  $v_{OB_a}$  is the velocity vector of the active osteoblast, which describes its migration within the cross-sectional slice. The local volume of osteoid  $\Delta V_{form}(r, t)$  "extruded" from the bone surface due to this displacement is given by the volume of a slanted cylinder, equal to the multiplication of its base

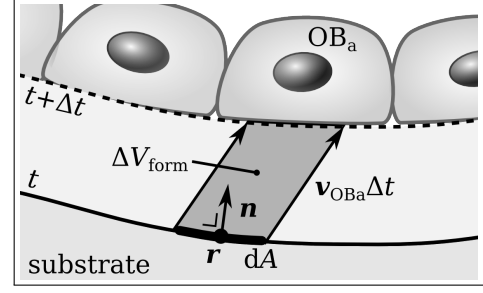


**Figure 6** – The displacement of the bone surface between time  $t$  and  $t + \Delta t$  can be described by the displacement  $v_{OB_a}\Delta t$  of the osteoblast ( $OB_a$ ) at point  $r$ . The volume "extruded" from the surface element  $dA$  between the times  $t$  and  $t + \Delta t$  due to this displacement is equal to  $n \cdot v_{OB_a} \Delta t dA$ . The normal component  $v_{form}^\perp \equiv n \cdot v_{OB_a}$  of the velocity vector corresponds to the matrix apposition rate.

$dA$  (a small, infinitesimal element of surface) and its height  $n(r, t) \cdot v_{OB_a}(r, t)\Delta t$ , where  $n(r, t)$  is a unit vector normal to the bone surface (see Figure 6). On the other hand,  $\Delta V_{form}(r, t)$  is given by the multiplication of the volume of osteoid produced per osteoblast per unit time  $k_{form}(r, t)$  and the number of active osteoblasts on the surface element  $dA$ . Introducing the surface density of active osteoblasts  $\rho_{OB_a}(r, t)$ , one thus has:

$$\Delta V_{form}(r, t) = n \cdot v_{OB_a} \Delta t dA = k_{form} \Delta t \rho_{OB_a} dA \quad (15)$$

The quantity  $v_{form}^\perp \equiv n \cdot v_{OB_a}$  describes the speed at which the bone surface moves in the direction normal to the surface. This quantity corresponds to the so-called 'matrix apposition rate', *i.e.*, the thickness of the new bone layer deposited per unit time. From Eq. (15), the matrix apposition rate at position  $r$  of the bone surface and at time  $t$  is therefore equal to:

$$v_{form}^\perp(r, t) = k_{form}(r, t) \rho_{OB_a}(r, t). \quad (5)$$

To estimate the overall rate at which the BMU cavity closes during the refilling process, one can integrate  $\Delta V_{form}(r, t)$  in Eq. (15) over the bone surface of the cross-sectional slice. This provides the total volume of osteoid produced in the slice during the time increment  $\Delta t$ . This newly-formed bone progressively closes the BMU cavity, of surface area  $S(x, t)$ . The change in  $S(x, t)$  is thus given by:

$$\Delta S(x, t) \delta x = - \int_P \Delta V_{form}(r, t) \delta x dl \quad (16)$$

where the small element of surface  $dA$  was replaced by  $dA = \delta x dl$  ( $dl$  is a length element of the cavity perimeter  $P$ ). Assuming that  $k_{form}$ ,  $v_{OB_a}$  and  $\rho_{OB_a}$  do not vary significantly within the cross section, these quantities can be taken out of the integral sign when using Eq. (15), and so we retrieve Eq. (3) and a special case of Eqs. (5) when  $\Delta t \rightarrow 0$ :

$$\begin{aligned} \frac{\partial}{\partial t} S(x, t) &= -k_{form}(x, t) \rho_{OB_a}(x, t) P(x, t) \\ &= -v_{form}^\perp(x, t) P(x, t) \end{aligned} \quad (3)$$

**Geometric influence of surface availability.** The tendency of cavity shrinkage to concentrate the density of osteoblasts is represented by the source term  $G_{OB_a}$  in the governing equation of active osteoblasts, Eq. (6). This effect can be understood intuitively as follows. During refilling, active osteoblasts move towards the center of the BMU as the cavity



radius decreases. This movement confines active osteoblasts into a smaller volume, and so tends to concentrate their density in the slice (see Figure 1b, stages 2–3). An alternative viewpoint is to note that the bone surface available to osteoblasts decreases as refilling proceeds. If the number of active osteoblasts on the surface is constant, this increases their surface density.

The precise form of the function  $G(x, t)$  can be determined by considering the total number of active osteoblasts in the slice,  $\delta N_{\text{OB}_a}(x, t)$ . This total number  $\delta N_{\text{OB}_a}$ , however, is not necessarily constant: active osteoblasts in the slice can be created or eliminated by biological processes. (Active osteoblasts are not transported into or away from the slice by migration from neighbouring slices since osteoblasts do not move along the  $x$  axis, see Section 2.1). In Eq. (6), biological creation or elimination of active osteoblasts in the slice is described in terms of changes in the volumetric density  $\text{OB}_a$  by the source and sink terms  $\sigma(x, t) \equiv \mathcal{D}_{\text{OB}_p} \text{OB}_p(x, t) - A_{\text{OB}_a} \text{OB}_a(x, t) - \sigma_{\text{OCY}}^{\text{prod.}}(x, t)$ . At the whole slice level, the number of active osteoblasts created or eliminated per unit time is therefore described by the source and sink terms  $\sigma(x, t) S_{\text{OB}_a}(x, t) \delta x$  since  $\delta N_{\text{OB}_a}(x, t) = \text{OB}_a(x, t) S_{\text{OB}_a}(x, t) \delta x$ , see Eq. (7). Hence:

$$\frac{\partial}{\partial t} \delta N_{\text{OB}_a} = \left[ \left( \frac{\partial}{\partial t} \text{OB}_a \right) S_{\text{OB}_a} + \text{OB}_a \frac{\partial}{\partial t} S_{\text{OB}_a} \right] \delta x = \sigma S_{\text{OB}_a} \delta x.$$

Dividing by  $S_{\text{OB}_a} \delta x$  and comparing the second equation with Eq. (6) gives:

$$G(x, t) = - \frac{\frac{\partial}{\partial t} S_{\text{OB}_a}(x, t)}{S_{\text{OB}_a}(x, t)} = - \frac{\frac{\partial}{\partial t} R(x, t)}{R(x, t) \left( 1 - \frac{h_{\text{OB}_a}}{2R(x, t)} \right)}. \quad (17)$$

In Eq. (17), the second equality is obtained using Eq. (8) and holds only for rotation-symmetric BMUs.

**Osteoblast-to-osteocyte transition.** The generation of osteocytes from osteoblasts that become entrapped in the bone matrix during bone formation [22, 52, 53] induces a sink term  $-\sigma_{\text{OCY}}^{\text{prod.}}(x, t)$  in the governing equation of active osteoblasts, Eq. (6). Here, we determine the rate  $\sigma_{\text{OCY}}^{\text{prod.}}(x, t)$  at which active osteoblasts become osteocytes (in units of density produced per unit time) so as to reproduce a given (*e.g.*, experimentally determined) osteocyte lacuna density in the cortical BMU,  $\text{OCY}_{\text{exp.}}(x, r)$ , where  $r$  is the radial coordinate in the cross section of the (rotation-symmetric) BMU (see Figure 1b). The total number of osteocytes in the slice at  $x$  at time  $t$ ,  $N_{\text{OCY}}(x, t)$ , increases during bone deposition in the slice from zero at the onset of bone refilling  $t = t_F$  (Figure 1b, stage 1) to a constant final number at the end of bone refilling (Figure 1b, stage 4). The correspondence between the given density  $\text{OCY}_{\text{exp.}}$  and the production rate of osteocytes  $\sigma_{\text{OCY}}^{\text{prod.}}$  is found by calculating  $N_{\text{OCY}}(x, t)$  separately from  $\text{OCY}_{\text{exp.}}$  and  $\sigma_{\text{OCY}}^{\text{prod.}}$ . The number of osteocytes in the slice  $N_{\text{OCY}}(x, t)$  is given on the one hand by spatially integrating the given density  $\text{OCY}_{\text{exp.}}$  from the cement line radius  $R_c$  up to the cavity radius at time  $t$ ,  $R(x, t)$  (Figure 1b), and on the other hand, by temporally integrating the production rate  $\sigma_{\text{OCY}}^{\text{prod.}}$  from the onset of formation  $t_F$  to  $t$ :

$$N_{\text{OCY}}(x, t) = 2\pi \int_{R(x, t)}^{R_c} dr r \text{OCY}_{\text{exp.}}(x, r) = \int_{t_F}^t dt' (\sigma_{\text{OCY}}^{\text{prod.}} S_{\text{OB}_a})(x, t')$$

Differentiating the above equation with respect to  $t$  then gives:

$$\begin{aligned} -2\pi R(x, t) \text{OCY}_{\text{exp.}}(x, R(x, t)) \frac{\partial}{\partial t} R(x, t) \\ = \sigma_{\text{OCY}}^{\text{prod.}}(x, t) S_{\text{OB}_a}(x, t), \end{aligned}$$

whence, using Eq. (8):

$$\sigma_{\text{OCY}}^{\text{prod.}}(x, t) = - \frac{\frac{\partial}{\partial t} R(x, t)}{h_{\text{OB}_a} \left( 1 - \frac{h_{\text{OB}_a}}{2R(x, t)} \right)} \text{OCY}_{\text{exp.}}(x, R(x, t)). \quad (18)$$

**Governing equations of cell densities and signalling molecules concentrations.** The densities of active osteoblasts ( $\text{OB}_a$ ), pre-osteoblast ( $\text{OB}_p$ ), and active osteoclasts ( $\text{OC}_a$ ), and the concentrations of the signalling molecules are governed by the material balance equation. Following Ref. [24], the signalling molecules considered in the model are transforming growth factor  $\beta$  ( $\text{TGF}\beta$ ), parathyroid hormone (PTH), and the receptor-activator nuclear factor  $\kappa\text{B}$  system comprising the receptor RANK, the ligand RANKL and the decoy receptor osteoprotegerin (OPG). The distribution profiles of uncommitted osteoblast progenitors (mesenchymal stem cells,  $\text{OB}_u(x, t)$ ) and of pre-osteoclasts ( $\text{OC}_p(x, t)$ ) are assumed to be given functions (see Table 3). Except for the dynamics of  $\text{TGF}\beta$ , which occurs on the same time scale as the resorption dynamics by active osteoclasts, the dynamics of the other signalling molecules is fast due to receptor-ligand reaction kinetics occurring on a much shorter time scale than the characteristic times of cell response. It can therefore be assumed that the concentrations of these signalling molecules quickly reach a pseudo-steady state (see Ref. [24] for a detailed discussion). This enables us to express the concentrations of PTH, RANKL, and OPG as algebraic equations.

Below we summarise all the equations governing the cell densities and the concentrations of signalling molecules in the model. The material balance equation governing the dynamics of active osteoblasts, Eq. (6), is rewritten using the explicit expressions in Eqs (17) and (18), and substituting  $\frac{\partial}{\partial t} R(x, t)$  by the right hand side of Eq. (10). We refer the reader to Ref. [24] for a detailed presentation of the derivation of the other equations:

$$\begin{aligned} \frac{\partial}{\partial t} \text{OB}_a(x, t) &= \mathcal{D}_{\text{OB}_p}(x, t) \text{OB}_p(x, t) - A_{\text{OB}_a} \text{OB}_a(x, t) \\ &\quad + k_{\text{form}}(x, t) \text{OB}_a(x, t) \left[ \frac{h_{\text{OB}_a}}{R(x, t)} \text{OB}_a(x, t) - \text{OCY}_{\text{exp.}}(x, R(x, t)) \right], \end{aligned} \quad (19)$$

$$\begin{aligned} \frac{\partial}{\partial t} \text{OC}_a(x, t) &= \mathcal{D}_{\text{OC}_p}(x, t) \text{OC}_p(x, t) - \mathcal{A}_{\text{OC}_a}(x, t) \text{OC}_a(x, t) \\ &\quad - \frac{\partial}{\partial x} (\text{OC}_a(x, t) v_{\text{OC}_a}), \end{aligned} \quad (20)$$

$$\frac{\partial}{\partial t} \text{OB}_p(x, t) = \mathcal{D}_{\text{OB}_u}(x, t) \text{OB}_u(x, t) - \mathcal{D}_{\text{OB}_p}(x, t) \text{OB}_p(x, t), \quad (21)$$

$$\frac{\partial}{\partial t} \text{TGF}\beta(x, t) = n_{\text{TGF}\beta}^{\text{bone}} k_{\text{res}} \text{OC}_a(x, t) - D_{\text{TGF}\beta} \text{TGF}\beta(x, t), \quad (22)$$

where

$$\mathcal{D}_{\text{OB}_p}(x, t) = D_{\text{OB}_p} \pi^{\text{rep}} \left( \frac{\text{TGF}\beta(x, t)}{k_{\text{OB}_p}^{\text{TGF}\beta}} \right), \quad (23)$$

$$\mathcal{D}_{\text{OC}_p}(x, t) = D_{\text{OC}_p} \pi^{\text{act}} \left( \frac{\text{RANKL}(x, t)}{k_{\text{OC}_p}^{\text{RANKL}}} \right), \quad (24)$$

$$\mathcal{A}_{\text{OC}_a}(x, t) = A_{\text{OC}_a} \pi^{\text{act}} \left( \frac{\text{TGF}\beta(x, t)}{k_{\text{OC}_a}^{\text{TGF}\beta}} \right), \quad (25)$$

$$\mathcal{D}_{\text{OB}_u}(x, t) = D_{\text{OB}_u} \pi^{\text{act}} \left( \frac{\text{TGF}\beta(x, t)}{k_{\text{OB}_u}^{\text{TGF}\beta}} \right), \quad (26)$$

and

$$PTH(x, t) = \beta_{PTH} / D_{PTH} \quad (27)$$

$$RANK(x, t) = N_{OC_p}^{RANK} OC_p(x, t) \quad (28)$$

$$OPG(x, t) = \frac{\beta_{OB_a}^{OPG} OB_a(x, t) \pi^{\text{rep}}\left(\frac{PTH(x, t)}{k_{OB, \text{rep}}^{PTH}}\right)}{\beta_{OB_a}^{OPG} OB_a(x, t) \pi^{\text{rep}}\left(\frac{PTH(x, t)}{k_{OB, \text{rep}}^{PTH}}\right) / OPG_{\text{sat}} + D_{OPG}} \quad (29)$$

$$RANKL(x, t) = \frac{\beta_{OB_p}^{RANKL} OB_p(x, t)}{1 + k_{RANK}^{RANKL} RANK(x, t) + k_{OPG}^{RANKL} OPG(x, t)} \times \left\{ D_{RANKL} + \frac{\beta_{OB_p}^{RANKL} OB_p(x, t)}{N_{OB_p}^{RANKL} OB_p(x, t) \pi^{\text{act}}\left(\frac{PTH(x, t)}{k_{OB, \text{act}}^{PTH}}\right)} \right\}^{-1} \quad (30)$$

The dimensionless functions  $\pi^{\text{act}}$  and  $\pi^{\text{rep}}$  express the activation and repression of cell differentiation, apoptosis, or ligand expression by regulatory signalling molecules. These functions are determined by the fraction of receptors on the cell occupied by the concerned signalling molecules (see Refs [24, 33]). Mathematically, they are ‘‘Hill’’ functions given by:

$$\pi^{\text{act}}(\xi) = \frac{\xi}{1 + \xi}, \quad \pi^{\text{rep}}(\xi) = 1 - \pi^{\text{act}}(\xi) = \frac{1}{1 + \xi}. \quad (31)$$

A slight change in the expression for RANKL in Eq. (30) has been made compared to Ref. [24]. The production of RANKL is now correctly proportional to the number of cells that express RANKL, *i.e.*, we have replaced  $\beta_{RANKL}$  in Ref. [24, Eq. (19)] by  $\beta_{OB_p}^{RANKL} OB_p$  in Eq. (30). The same inconsistency of having a production rate of RANKL not scaled by the number of osteoblasts is present in Ref. [33], which was corrected in Ref. [35]. The behaviour of the BMU model is not changed significantly by this correction. Some inconsistent behaviours of the temporal-only model of Ref. [33] were corrected by this change, see Ref. [35] for more details.

The set of equations (19)–(31) together with Eq. (10) are solved in a co-moving frame attached to the BMU with the following boundary conditions: the density of pre-osteoblasts and active osteoblasts is zero at the (moving) front of the BMU, and the density of active osteoclasts is zero at the back of the BMU (set at a distance of 5 mm behind the front of the BMU). The numerical algorithm used is that of the ‘method of lines’ of Mathematica’s NDSolve function.

**Scaling of the cell density distributions in the BMU.** In the Results section (Section 3), the cell distribution profiles along  $x$  resulting from the numerical simulation are calibrated against experimental values of osteoblast surface densities and total cell numbers. To this effect, we have modified the values of a number of parameters compared to the parameters used in Ref. [24] (that were themselves taken from Ref. [33]). We used a scaling scheme of the model parameters such that the densities of  $OB_a$ ,  $OB_p$ ,  $OB_u$ ,  $OC_a$  and  $OC_p$  would scale uniformly without affecting much their own spatial distribution and without affecting their spatial relation with other cell density profiles. We defined scaling factors  $\alpha_{OB_a}$ ,  $\alpha_{OB_p}$ ,  $\alpha_{OB_u}$ ,  $\alpha_{OC_a}$  and  $\alpha_{OC_p}$ , such that if  $\alpha_{OB_a} = 500$ , the density of  $OB_a$ s is

multiplied by a factor 500 etc. Based on Eqs (19)–(30), the new parameter values (denoted below by a prime) ensuring such scaled densities were determined by multiplying the previous parameter values with an adequate combination of the above scaling factors, according to:

$$\begin{aligned} OB_u^{\text{max}'} &= \alpha_{OB_u} OB_u^{\text{max}}, & OC_p^{\text{max}'} &= \alpha_{OC_p} OC_p^{\text{max}}, \\ D'_{OB_u} &= \frac{\alpha_{OB_p}}{\alpha_{OB_u}} D_{OB_u}, & D'_{OC_p} &= \frac{\alpha_{OC_a}}{\alpha_{OC_p}} D_{OC_p}, \\ n_{TGF\beta}^{\text{bone}'} &= n_{TGF\beta}^{\text{bone}} / \alpha_{OC_a}, & N_{OC_p}^{\text{RANK}'} &= N_{OC_p}^{\text{RANK}} / \alpha_{OC_p}, \\ \beta_{OB_a}^{\text{OPG}'} &= \beta_{OB_a}^{\text{OPG}} / \alpha_{OB_a}, & \beta_{OB_p}^{\text{OPG}'} &= \beta_{OB_p}^{\text{OPG}} / \alpha_{OB_p}, \\ N_{OB_p}^{\text{RANKL}'} &= N_{OB_p}^{\text{RANKL}} / \alpha_{OB_p}, & N_{OB_a}^{\text{RANKL}'} &= N_{OB_a}^{\text{RANKL}} / \alpha_{OB_a}, \end{aligned} \quad (32)$$

where  $OB_u^{\text{max}}$  and  $OC_p^{\text{max}}$  denote parameters scaling the given distributions of  $OB_u$ s and  $OC_p$ s [24]. We note that it is not possible to control the scaling of  $OB_p$  independently from that of  $OB_a$  without affecting their spatial relationship, and so we have always taken  $\alpha_{OB_p} = \alpha_{OB_a}$ .

**Table 3** – Model parameters and given functions

Symbol	Value	Description
$OC_p(x, t)$	(given function)	pre-osteoclast density: gaussian function centred at $x(t) = -0.35 \text{ mm} + v_{OC_a} t$ , with standard deviation = 0.2 mm and amplitude = 2589/mm <sup>3</sup> .
$OB_u(x, t)$	(given function)	uncommitted osteoblast progenitors (MSC) density, equal to $OC_p(x, t)$
$k_{form}(R)$	(given function)	volume of osteoid formed per osteoblast per day (see Figure 2)
$D_{OC_p}$	41.26/day	$OC_p \rightarrow OC_a$ differentiation rate parameter
$A_{OC_a}$	2.82/day	$OC_a$ apoptosis rate parameter
$D_{OB_u}$	81.07/day	$OB_u \rightarrow OB_p$ differentiation rate parameter
$D_{OB_p}$	0.166/day	$OB_p \rightarrow OB_a$ differentiation rate parameter
$A_{OB_a}$	0.0385/day	$OB_a$ apoptosis rate
$k_{OC_p}^{RANKL}$	$1.0025 \cdot 10^7 \text{ mm}^{-3}$	parameter for RANKL binding on $OC_p$
$k_{OC_a}^{TGF\beta}$	$339.2 \text{ mm}^{-3}$	parameter for TGF $\beta$ binding on $OC_a$
$k_{OB_u}^{TGF\beta}$	$339.2 \text{ mm}^{-3}$	parameter for TGF $\beta$ binding on $OB_u$
$k_{OB_p}^{TGF\beta}$	$105.6 \text{ mm}^{-3}$	parameter for TGF $\beta$ binding on $OB_p$
$k_{OB,act}^{PTH}$	$9.033 \cdot 10^7 \text{ mm}^{-3}$	parameter for PTH binding on OB (for $\pi^{act}$ )
$k_{OB,rep}^{PTH}$	$134039 \text{ mm}^{-3}$	parameter for PTH binding on OB (for $\pi^{rep}$ )
$k_{RANK}^{RANKL}$	$5.6655 \cdot 10^{-8} \text{ mm}^3$	association binding constant for RANKL and RANK
$k_{OPG}^{RANKL}$	$1.66058 \cdot 10^{-9} \text{ mm}^3$	association binding constant for RANKL and OPG
$\beta_{OB_p}^{RANKL}$	348.377/day	production rate of RANKL per $OB_p$
$\beta_{OB_a}^{OPG}$	326305/day	production rate of OPG per $OB_a$
$\beta_{PTH}$	$1.506 \cdot 10^8 \text{ mm}^{-3}/\text{day}$	production rate of systemic PTH
$N_{OB_p}^{RANKL}$	$2.7 \cdot 10^6$	maximum number of RANKL per $OB_p$
$N_{OC_p}^{RANK}$	2326	number of RANK receptors per $OC_p$
$OPG_{sat}$	$1.205 \cdot 10^{14} \text{ mm}^{-3}$	OPG density at which endogeneous production stops
$D_{TGF\beta}$	0.5/day	degradation rate of TGF $\beta$
$D_{RANKL}$	10.13/day	degradation rate of RANKL
$D_{OPG}$	0.35/day	degradation rate of OPG
$D_{PTH}$	86/day	degradation rate of PTH
$n_{TGF\beta}^{bone}$	$3946 \text{ mm}^{-3}$	concentration of TGF $\beta$ stored in the bone matrix
$k_{res}$	$9.425 \cdot 10^{-6} \text{ mm}^3/\text{day}$	volume of bone matrix resorbed per osteoclast per day
$v_{OC_a}$	30 $\mu\text{m}/\text{day}$	longitudinal speed of active osteoclasts and of the BMU
$R_H$	20 $\mu\text{m}$	human Haversian canal radius
$R_c$	100 $\mu\text{m}$	human cement line radius
$h_{OB_a}$	15 $\mu\text{m}$	average height of an active osteoblast
$\alpha_{k_{form}}$	1.25	canine-to-human conversion factor for osteoid secretion rate
$\rho_{LC}$	2300/mm <sup>2</sup>	surface density of bone lining cells
$OCY_{exp.}(x, r)$	20000/mm <sup>3</sup>	volumetric density of osteocyte lacunae in the BMU

## References

- [1] Martin RB, Burr DB and Sharkey NA (1998). *Skeletal tissue mechanics* (New York: Springer)
- [2] Parfitt A M (1994) Osteonal and hemi-osteonal remodeling: the spatial and temporal framework for signal traffic in adult human bone. *J. Cell. Biochem.* **55**:273–286
- [3] Manolagas S (2000) Birth and death of bone cells: Basic regulatory mechanisms and implications for the pathogenesis and treatment of osteoporosis, *Endocr Rev* **21**:115–137
- [4] Jilka RL (2003) Biology of the basic multicellular unit and the pathophysiology of osteoporosis, *Med Pediatr Oncol* **41**:182–185
- [5] Seeman E (2008) Modeling and remodeling: The cellular machinery responsible for the gain and loss of bone's material and structural strength. In Bilezikian JP, Raisz LG and Martin TJ, editors. *Principles of bone biology*. 3rd ed: Elsevier.
- [6] Jilka RL (2002) Osteoblast progenitor fate and age-related bone loss, *J Musculoskel Neuron Interact* **2**:581–583
- [7] van Bezooijen RL, Papapoulos SE, Hamdy NAT, Löwik CWGM (2008) SOST/Sclerostin: An osteocyte-derived inhibitor of bone formation that antagonizes canonical Wnt signaling. In Bilezikian JP, Raisz LG and Martin TJ, editors. *Principles of bone biology*. 3rd ed: Elsevier.
- [8] Harada S-I and Rodan G A (2003) Control of osteoblast function and regulation of bone mass. *Nature* **423**:349–355
- [9] Frost HM (1969) Tetracycline-based histological analysis of bone remodeling, *Calc Tiss Res* **3**:211–237
- [10] Eriksen EF, Axelrod DW, Melsen F (1994) *Bone histomorphometry* (Raven Press: New York)
- [11] Lee WR (1964) Appositional bone formation in canine bone: a quantitative microscopic study using tetracycline markers, *J Anat Lond* **98**:665–677
- [12] Manson JD and Waters NE (1965) Observations on the rate of maturation of the cat osteon, *J Anat Lond* **99**:539–549
- [13] Ilnicki L, Epker BN, Frost HM, Hattner R (1966) The radial rate of osteon closure evaluated by means of in vivo tetracycline labeling in beagle dog rib, *J Lab Clin Med* **67**:447–454
- [14] Hood SJ, Morrin LA, Parks NJ, Bugreeff SE (1985) Bone histomorphometry: analysis of results of juvenile cortical bone study. Annual Report Laboratory for Energy-Related Health Research, UC Davis, pp 70–75
- [15] Martin RB, Dannucci GA, Hood SJ (1987) Bone apposition rate differences in osteonal and trabecular bone, *Trans Orth Res Soc* **12**:178
- [16] Metz LN, Martin RB and Turner AS (2003) Histomorphometric analysis of the effects of osteocyte density on osteonal morphology and remodeling, *Bone* **33**:753–759
- [17] Jones SH (1974) Secretory territories and rates of matrix production of osteoblasts, *Calc Tiss Res* **14**:309–315
- [18] Marotti G, Zamboni Zallone A and Ledda M (1976) Number, size and arrangement of osteoblasts in osteons at different stages of formation. *Calcif. Tissue Int.* **21**(suppl):96–101
- [19] Volpi G, Palazzini S, Cané V, Remaggi F, Muglia MA (1981) Morphometric analysis of osteoblast dynamics in the chick embryo tibia, *Anat Embryol* **162**:393–401
- [20] Qiu S, Rao DS, Palnitkar S, Parfitt AM (2010) Dependence of bone yield (volume of bone formed per unit of cement surface area) on resorption cavity size during osteonal remodeling in human rib: Implications for osteoblast function and the pathogenesis of age-related bone loss, *J Bone Miner Res* **25**:423–430
- [21] Martin RB (2000) Does osteocyte formation cause the nonlinear refilling of osteons? *Bone* **26**:71–78
- [22] Marotti G (2000) The osteocyte as a wiring transmission system, *J Musculoskel Neuron Interact* **1**:133–136
- [23] Rumpler M, Woesz A, Dunlop J W C, van Dongen J T and Fratzl P (2008) The effect of geometry on three-dimensional tissue growth. *J. R. Soc. Interface* **5**:1173–1180
- [24] Buenzli PR, Pivonka P, Smith DW (2011) Spatio-temporal structure of cell distribution in bone multicellular units, *Bone* **48**:918
- [25] Zamboni Zallone A (1977) Relationships between shape and size of the osteoblasts and the accretion rate of trabecular bone surfaces, *Anat Embryol* **152**:65–72
- [26] MH Zheng, Bruining HG, Cody SH, Brankov B, Wood DJ, Papadimitriou JM (1997) A rapid method for the assessment of bone architecture by confocal microscopy. *Histochem J* **29**:639–643
- [27] Jaworski Z F G, Duck B and Sekaly G (1981) Kinetics of osteoclasts and their nuclei in evolving secondary Haversian systems. *J. Anat.* **133**:397–405
- [28] Aubin JE (2008) Mesenchymal stem cells and osteoblast differentiation. In Bilezikian JP, Raisz LG and Martin TJ, editors. *Principles of bone biology*. 3rd ed: Elsevier.
- [29] Pazzaglia UE, Congiu T, Marchese M, Dell'Orbo C (2010) The shape modulation of osteoblast–osteocyte transformation and its correlation with the fibrillar organization in secondary osteons, *Cell Tissue Res* **340**:533–540
- [30] Pazzaglia UE, Congiu T, Franzetti E, Marchese M, Spagnuolo F, Di Mascio L, Zarattini G (2012) A model of osteoblast–osteocyte kinetics in the development of secondary osteons in rabbits, *J Anat* **220**:372–383
- [31] Parfitt AM (1983) The physiological and clinical significance of bone histomorphometric data. In Recker RR (Ed.), *Bone histomorphometry: Techniques and interpretation*. CRC Press, Boca Raton, pp. 143–223.
- [32] Komarova SV, Smith RJ, Dixon SJ, Sims SM, Wahl LM (2003) Mathematical model predicts a critical role for osteoclast autocrine regulation in the control of bone remodeling, *J Theor Biol* **229**:293–309
- [33] Pivonka P *et al.* (2008) Model structure and control of bone remodeling: a theoretical study. *Bone* **43**:249–263
- [34] van Oers RFM, van Rietbergen B, Ito K, Huiskes R, Hilbers PAJ (2011) Simulations of trabecular remodeling and fatigue: Is remodeling helpful or harmful? *Bone* **48**:1210–1215
- [35] Buenzli PR, Pivonka P, Gardiner BS, Smith DW (2012) Modelling the anabolic response of bone using a cell population model, *J Theor Biol* **307**:42–52
- [36] Pivonka P, Buenzli PR, Scheiner S, Hellmich Ch, Dunstan CR (2012) The influence of bone surface availability in bone remodelling—A mathematical model including coupled geometrical and biomechanical regulations of bone cells. Preprint: [arXiv:1112.5685](https://arxiv.org/abs/1112.5685)
- [37] Buenzli PR, Thomas CDL, Clement JG, Pivonka P (2012) Endocortical bone loss in osteoporosis: The role of bone surface availability. Preprint: [arXiv:1206.6071](https://arxiv.org/abs/1206.6071)
- [38] Polig E and Jee W S S (1990) A model of osteon closure in cortical bone. *Calcif. Tissue Int.* **47**:261–269
- [39] Ryser M D, Nigam N and Komarova S V 2009 Mathematical modeling of spatio-temporal dynamics of a single bone multicellular unit. *J. Bone Miner. Res.* **24**:860–870
- [40] Ryser M D, Komarova S V and Nigam N 2010. The cellular dynamics of bone remodelling: a mathematical model. *SIAM J. Appl. Math.* **70**:1899–1921
- [41] van Oers RFM, Ruimerman R, Tanck E, Hilbers PAJ, Huiskes R (2008) A unified theory for osteonal and hemi-osteonal remodeling. *Bone* **42**:250–259
- [42] Ji B, Genever PG, Patton RJ, Putra D and Fagan MJ (2012) A novel mathematical model of bone remodelling cycles for trabecular bone at the cellular level. In Press, *Biomech Model Mechanobiol.*
- [43] Buenzli PR, Jeon J, Pivonka P, Smith DW, Cummings PT (2012), Investigation of bone resorption within a cortical basic multicellular unit using a lattice-based computational model, *Bone* **50**:378



- [44] van Kampen NG (2007) *Stochastic processes in physics and chemistry*. 3<sup>rd</sup> Ed (Elsevier)
- [45] Frost HM (1963) Measurement of human bone formation by means of tetracycline labelling, *Can J Biochem Physio* **41**:31–42
- [46] Lindsay R, Cosman F, Zhou H, Bostrom MP, Shen VW, Cruz JD, Nieves JW, Dempster DW (2006) A novel tetracycline labeling schedule for longitudinal evaluation of the short-term effects of anabolic therapy with a single iliac crest bone biopsy: Early actions of teriparatide, *J Bone Miner Res*: **21**:366–373
- [47] Jowsey (1966) Studies of Haversian systems in man and some animals, *J Anat* **100**:857–864
- [48] Jaworski Z F G and Hooper C (1980) Study of cell kinetics within evolving secondary haversian systems. *J. Anat. London* **131**:91–102
- [49] Robling AG and Stout SD (1998) Morphology of the drifting osteon, *Cells Tissues Organs* **164**:192–204
- [50] Cohen J, Harris WH (1958) The three-dimensional anatomy of Haversian systems. *J Bone Joint Surg Am* **40**:419–434
- [51] Cooper DM, Thomas CDL, Clement JG, Hallgrímsson B (2006) Three-dimensional microcomputed tomography imaging of basic multicellular unit-related resorption spaces in human cortical bone. *Anat Rec A Discov Mol Cell Evol Biol* **288A**:806–816.
- [52] Franz-Odenaal T A, Hall B K and Witten P E (2006) Buried alive: How osteoblasts become osteocytes. *Developmental Dynamics* **235**:176–190
- [53] Dallas SL, Bonewald LF (2010) Dynamics of the transition from osteoblast to osteocyte, *Ann N Y Acad Sci* **1192**:437–443